

Harvesting Vibration Energy and Wind Energy by a Bi-stable Harvester: Modeling and Experiments

Haitao Li (✉ haitaolee@mail.nwpu.edu.cn)

North University of China <https://orcid.org/0000-0003-0211-408X>

Bojian Dong

North University of China

Fan Cao

North University of China

Weiyang Qin

NWPU: Northwestern Polytechnical University

Hu Ding

Shanghai University

Liqun Chen

Shanghai University

Research Article

Keywords: bi-stable energy harvester, snap-through, galloping, base excitations

Posted Date: June 12th, 2021

DOI: <https://doi.org/10.21203/rs.3.rs-572949/v1>

License:   This work is licensed under a Creative Commons Attribution 4.0 International License.

[Read Full License](#)

Harvesting vibration energy and wind energy by a bi-stable harvester: Modeling and experiments

Hai-Tao Li^{1,2}, Bo-Jian Dong¹, Fan Cao¹, Wei-Yang Qin³, Hu Ding², Li-Qun Chen²

1. Department of Engineering Mechanics, North University of China, Taiyuan, 030051, China

2. Shanghai Institute of Applied Mathematics and Mechanics, Shanghai University, Shanghai, 200072, China;

3. Department of Engineering Mechanics, Northwestern Polytechnical University, Xi'an, 710072, China

Abstract

In realistic environments, there often appears the concurrence of base excitation and blowing wind. Harvesting both vibration energy and wind energy by an unique harvester is attractive. In this paper, we proposed a harvester integrating bi-stability and galloping to realize this aim. The nonlinear dynamical model of the bistable energy harvester under concurrent wind and base excitations is established. The galloping effects on the responses are explored based on the established model, for both harmonic and random excitations. The corresponding experiments are conducted to validate the theoretical prediction. The experimental results are consistent with the simulation results. At a wind speed of $U=2$ m/s, the bandwidth of large-amplitude inter-well motion of the bi-stable energy harvester is extended by about 18.5%. The critical random excitation level for snap-through is reduced by 58% and the total output voltage at random excitation is increased by 53.4%. Thus, the harvester could scavenge the wind and vibration energies at a high efficiency. These conclusions could be helpful for improving the harvesting efficiency in the real environment.

Keywords: bi-stable energy harvester, snap-through, galloping, base excitations.

E-mails: Hai-Tao Li <haitaolee@mail.nwpu.edu.cn>,

Bo-Jian Dong <1007956811@qq.com>,

Fan Cao <743515885@qq.com>,

Wei-Yang Qin <qinweiyang@nwpu.edu.cn>,

Hu Ding <dinghu3@shu.edu.cn>,

Li-Qun Chen <lqchen@shu.edu.cn>.

1. Introduction

At present, the general solutions for powering wireless sensors are dependent on electrochemical batteries. However, this may bring about some derived problems, such as manual maintenance costs and unavoidable environmental pollution. Vibration, as a common ambient source, is ubiquitous in the nature. Vibration energy harvesting (VEH), which converts ambient vibration energy to electrical energy, has received a significant amount of attention [1-2]. Many earlier works focused on the scheme exploiting the linear resonance. Unfortunately, the response's amplitudes of such designs will drop significantly if the external exciting frequency does not match with the natural frequency of the structure [3-5]. As is well known, the ambient vibration has the feature of weak intensity and broad bandwidth. Therefore, increasing the harvester's adaptability to the broadband environment excitation is significantly important.

To achieve a broad bandwidth, the active frequency tuning method [6, 7], passive frequency tuning method [8-10], and multimodal structure [11] are proposed. In recent years, nonlinear energy harvesting emerged and developed, as a potential solution for achieving high performance. Numerous nonlinear characteristics, such as hardening [12-15], softening [16] and impact [17] are introduced to the design of energy harvesters.

As a typical nonlinear system, the bi-stable energy harvester has received much attention because of its broadband property and high voltage output upon the occurrence of snap-through [18-24]. Stanton et al. [25] proposed a bi-stable energy harvester based on the magnetic repulsion and characterize its complex nonlinear dynamics behaviors. Erturk et al. [26] presented a bi-stable energy harvester with external attraction magnets. Cao et al. [27] carried out numerical and experimental investigations on a bi-stable energy harvester with two external rotational magnets. The results verified it was preferred to the linear and mono-stable energy harvesters from harmonic base excitation.

Since ambient sources may influence the behavior of energy harvester, some

researchers investigate the response of energy harvesting systems under non-harmonic excitation [28, 29]. The ambient vibration is usually described as a random process, which has a wide spectrum. Cottone et al. [30] theoretically modeled a bi-stable energy harvester by considering the axial load and experimentally investigated the response under random excitations. As the axial force exceeds the critical buckling load of a beam, the system generated more electrical energy. Zhao and Erturk [31] investigated the relative advantage of mono-stable and bi-stable energy harvester. If only the level of excitation is above the critical value of inter-well oscillation, the bi-stable energy harvester captured more energy. Fang et al. [32] proposed an asymmetric plucking-based bi-stable energy harvester with rotary structure and plectrum, to convert the impulsive excitation to plucking force that helps the harvester jump into the high-energy orbit.

In the nature, the flowing river and air own a huge amount of kinetic energy, transforming which to electric energy has a realistic significance. Galloping energy harvester has attracted a great deal of attention, because it can oscillate dramatically if the speed of wind exceeds the critical onset one [33-39]. Dai et al. [40, 41] developed a distributed-parameter model of an electromagnetic galloping energy harvester, and the effect of magnet displacement and electromagnetic coupling is investigated by a parametric analysis. Zhou et al. [42] proposed a Y-shape bi-stable energy harvester to scavenge the low-speed wind energy.

To improve the harvesting efficiency, the energy harvesters under the hybrid excitations of galloping and base motion are investigated by some researchers [43-46]. Most researches related to galloping-based energy harvesters considered linear stiffness, and up till now, few works devoted themselves to investigate the interaction between the base excitation and galloping [46, 47]. Zhao et al. [48] introduced the impact into the design of aeroelastic energy harvesters, and the results demonstrated a broadened bandwidth for concurrent wind and vibration energy harvesting. In fact, vibration energy harvester in the real environment is inevitably disturbed by the flow of air, but the effect of galloping on the bi-stable energy harvester under random excitation is still not clear. Thus, exploring the effect of galloping on the bi-stable

energy harvester will provide new insight and improve energy harvesting performance.

In this paper, the effect of galloping on the bi-stable energy harvesting system has been investigated. The rest of this manuscript is organized as follows. Section 2 provided the process of modeling. In Section 3, numerical simulations are carried out to compare and analyze the response under base excitation solely and combined base excitation and galloping. In Section 4, experimental verification is performed at different excitations to study the effect of galloping on bi-stable energy harvesters. The result obtained from the experiment accords with the numerical simulation, which demonstrates the positive effect of galloping on a bi-stable energy harvester. Summary and conclusions are presented in Section 5.

2. Designing and Modeling

As shown in **Figure 1**, the bi-stable piezoelectric energy harvester is composed of a steel cantilever beam of length L and a piezoelectric layer (Macro-fiber composites: MFC), which is characterized by length L_p , width w_p , thickness h_p , electro-mechanical coupling coefficient e_{31} and permittivity e_{33} . The piezoelectric layer is connected to an electrical impedance R . A NdFeB magnet is fixed at the top of the cantilever beam, while two magnets are mounted on the fixture. Moreover, at the free end of the cantilever beam is attached a half-cylinder bluff body of mass M_E , which can induce galloping in the flowing wind. Then, owing to the coexistence of base motion and wind, the harvester is subjected to the combined excitation of base motion $y(t)$ and galloping force $F_{\text{galloping}}(t)$. The aerodynamic model is established using the quasi-steady hypothesis, while the galloping aerodynamics force is given by [37, 45]

$$F_{\text{galloping}} = \frac{1}{2} \rho_a D_B L_B U^2 \sum_{i=1}^3 a_i \left(\frac{\dot{x} + y}{U} \right)^i \quad (1)$$

where ρ_a is the air density, L_B and D_B are the length and diameter of the bluff

body, respectively. U is the incoming wind speed, a_i ($i=1, 2, 3$) are the empirical coefficients, which can be obtained by a polynomial fitting for the total aerodynamical force in the cross-flow direction and the tangential direction of angle of attack. w represents the transverse displacement, and " \cdot " represents the derivative with respect to time t .

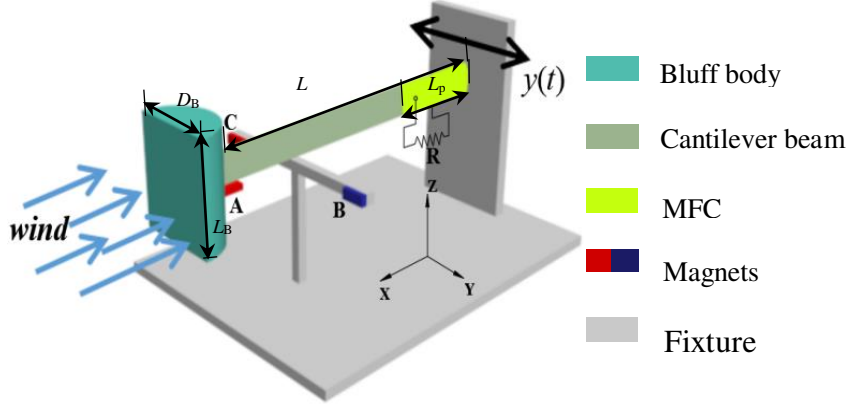


Figure 1. Configuration of proposed energy harvester subjected to concurrent wind and base excitation.

The total kinetic and potential energies can be given by

$$T = \frac{1}{2} \left[\int_0^L m_b (\dot{w} + \dot{y})^2 dx + \int_0^{L_p} m_p (\dot{w} + \dot{y})^2 dx \right] + \frac{1}{2} M_E (w_{x=L} + y)^2, \quad (2)$$

$$U = U_{bp} + U_M$$

$$= \frac{1}{2} Y_b I_b \int_0^L w''^2 dx + C_{11}^E I_p \int_0^{L_p} w''^2 dx - \frac{1}{2} e_{31} V (h_b + h_p) b w'_{x=L_p} - \frac{1}{4} C_p V^2 + U_M, \quad (3)$$

where m_b and m_p are the masses per unit length of steel beam and piezoelectric patches, respectively; U_{bp} and U_M refer to the potential energy of beam and the one induced by the magnetic force, respectively; $Y_b I_b$ and $C_{11}^E I_p$ represent the flexural rigidities of beam and piezoelectric patches, respectively. " $'$ " denotes the derivative with respect to x . $C_p = e_{33} w_p L_p / h_b$ is the capacitance of the piezoelectric patches. h_b is the thickness of beam. $V(t)$ is the voltage generated by the piezoelectric layers.

As shown in **Figure 2(a)**, to obtain the potential energy produced by magnetic forces, the permanent magnets in the structure are modeled as the point dipoles, the distance between magnets B and C is $2a$, while the one between magnet A and the pedestal is denoted by d . The extensibility condition is used to relate the longitudinal

displacement u_1 with the transverse displacement via $u_1 = \frac{1}{2} \int_0^L (w')^2 dx$.

The magnetic moment vector $\boldsymbol{\mu}_j (j = A, B, C)$ is proportional to the volume of magnet $V_{m_j} (j = A, B, C)$, $\boldsymbol{\mu}_j = M_j V_{m_j} (j = A, B, C)$. Based on the orthogonal decomposition, the magnetic dipole moment vectors can be written as

$$\boldsymbol{\mu}_A = -M_A V_{mA} \sin \theta \hat{\mathbf{e}}_x + M_A V_{mA} \cos \theta \hat{\mathbf{e}}_y, \quad (4a)$$

$$\boldsymbol{\mu}_B = -M_B V_{mB} \hat{\mathbf{e}}_x, \quad (4b)$$

$$\boldsymbol{\mu}_C = M_C V_{mC} \hat{\mathbf{e}}_x, \quad (4c)$$

where $M_j (j = A, B, C)$ represents the vector sum of all microscopic magnetic moments of ferromagnetic material, $V_{m_j} (j = A, B, C)$ is the volume of magnets; $\hat{\mathbf{e}}_x$ and $\hat{\mathbf{e}}_y$ are the unit vectors parallel to x - and y - axis, respectively. The rotate angle θ can be obtained from the approximation relation, $\tan \theta \approx \frac{\partial w}{\partial x}$.

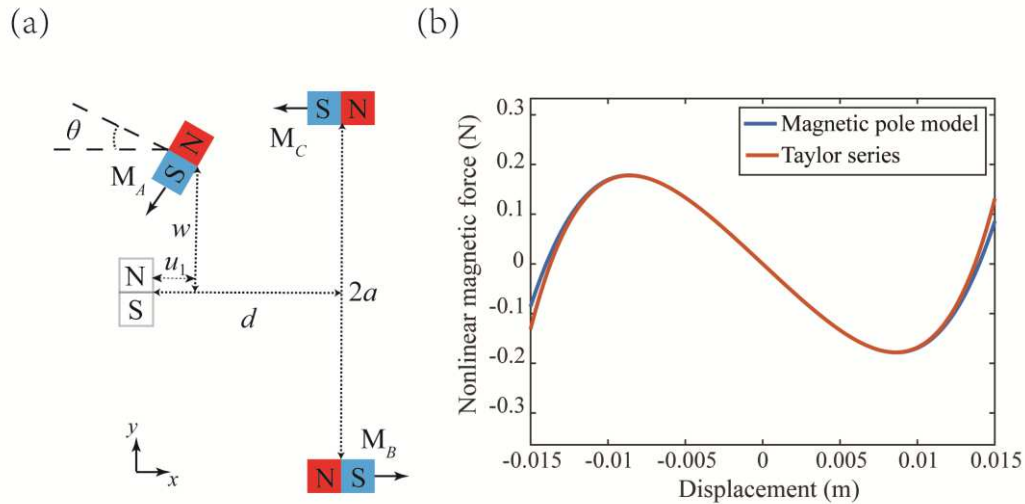


Figure 2. (a) Geometric diagram of magnetic dipoles; (b) Nonlinear magnetic force.

The magnetic fields acting on dipole A by dipoles B and C can be given by

$$\mathbf{B}_{BA} = -\frac{\mu_0}{4\pi} \nabla \frac{\boldsymbol{\mu}_B \cdot \mathbf{r}_{BA}}{|\mathbf{r}_{BA}|^3}, \quad \mathbf{B}_{CA} = -\frac{\mu_0}{4\pi} \nabla \frac{\boldsymbol{\mu}_C \cdot \mathbf{r}_{CA}}{|\mathbf{r}_{CA}|^3}, \quad (5)$$

where $\mu_0 = 4\pi \times 10^{-7} \text{ H/m}$ is the magnetic permeability constant. $|\cdot|_2$ and ∇ denote the Euclidean norm and vector gradient operator, respectively. According to the

geometrical orientation, the vectors directed from the fixed magnets B and C to the tip magnet A can be expressed as

$$\mathbf{r}_{BA} = (d - u_1)\hat{\mathbf{e}}_x - (a - w)\hat{\mathbf{e}}_y, \quad \mathbf{r}_{CA} = (d - u_1)\hat{\mathbf{e}}_x + (a + w)\hat{\mathbf{e}}_y. \quad (6)$$

Then, the potential energy of magnetic field can be written as [34]:

$$U_m = -\boldsymbol{\mu}_A \mathbf{B}_{BA} - \boldsymbol{\mu}_A \mathbf{B}_{CA} \\ = \frac{\mu_0}{4\pi} \boldsymbol{\mu}_A \left[\left(\frac{\boldsymbol{\mu}_B}{|\mathbf{r}_{BA}|^3} - \frac{3(\boldsymbol{\mu}_B \cdot \mathbf{r}_{BA})\mathbf{r}_{BA}}{|\mathbf{r}_{BA}|^5} \right) + \left(\frac{\boldsymbol{\mu}_C}{|\mathbf{r}_{CA}|^3} - \frac{3(\boldsymbol{\mu}_C \cdot \mathbf{r}_{CA})\mathbf{r}_{CA}}{|\mathbf{r}_{CA}|^5} \right) \right]. \quad (7)$$

Supposing that the first mode is dominant in the Galerkin expansion, the transverse displacement can be expressed as

$$w = q\psi(x), \quad (8)$$

where q is the generalized time-dependent modal coordinate, and $\psi(x)$ is the first mode shape of the beam and can be given by $\psi(x) = 1 - \cos\left(\frac{\pi x}{2L}\right)$ [8].

To derive the dynamical equation of the system, Lagrangian equations are employed, which has the form as follows:

$$\frac{d}{dt} \left(\frac{\partial L}{\partial \dot{\phi}} \right) - \frac{\partial L}{\partial \phi} = F, \\ \frac{d}{dt} \left(\frac{\partial L}{\partial \dot{V}} \right) - \frac{\partial L}{\partial V} = Q, \quad (9)$$

where $L = T - U_M - U_{bp}$ is the Lagrangian; F is the nonconservative force, which includes two parts, the galloping excitation $F_{\text{galloping}}$ and the damping force $F_{\xi} = 2M\xi\omega_1$. In the damping force, M is the modal mass, ξ is the equivalent damping ratio, and ω_1 is the natural frequency. Q is the electric charge of piezoelectric layer, and the electric current passing through the resistive load R is expressed by $\dot{Q} = V/R$.

The nonlinear model of the piezoelectric energy harvester subjected to concurrent galloping and base excitations can be derived to give

$$M\ddot{\phi} + 2M\xi\omega_1\dot{\phi} + Kq + F_m - \theta V = -N\ddot{y}_b + \frac{1}{2}\rho_a D_B L_B U^2 \sum_{i=1}^3 a_i \left(\frac{w + \dot{Q}}{U} \right)^i, \\ \frac{1}{2}C_p \dot{V} + \frac{V}{R} + \theta\dot{\phi} = 0, \quad (10)$$

where K is the equivalent stiffness. F_m is the nonlinear magnetic force, which can be obtained by the formula as $\partial U_m / \partial x$. θ is the equivalent electro-mechanical coupling coefficient. N represents the coefficients of the first mode of external force due to the base excitation. C_p is the capacitance of piezoelectric materials (MFC). These coefficients can be evaluated by the following formulas:

$$M = m_b \int_0^L (\psi(x))^2 dx + m_p \int_0^{L_p} (\psi(x))^2 dx + M_E [\psi(x)]^2 \Big|_{x=L},$$

$$K = Y_b I_b \int_0^L [\psi(x)'']^2 dx + 2C_{11}^E I_p \int_0^{L_p} [\psi(x)'']^2 dx,$$

$$\theta = \frac{1}{2} w_b e_{31} (h_b + h_p) \psi(x)' \Big|_{x=L_p},$$

$$N = \rho_b A_b \int_0^L \psi(x) dx + \rho_p A_p \int_0^{L_p} \psi(x) dx + M_E \psi(x) \Big|_{x=L}.$$

Specifically, the nonlinear magnetic force F_m can be approximated by the Taylor series

$$F_m = K_1 q + K_2 q^3 + K_3 q^5. \quad (11)$$

To prove the accuracy of **Eq. (11)**, in **Figure 2(b)**, the nonlinear magnetic force obtained from the magnetic pole model and **Eq. (11)** are compared. It is clear that the polynomial approximation (In **Eq. (11)**, $K_1=-26.1$, $K_2=4.0 \times 10^3$ and $K_3=1.6 \times 10^8$) could reach a high accuracy. Thus, the governing equation (10) can be rewritten as

$$M \ddot{q} + 2M \xi \omega_1 \dot{q} + (K + K_1)q + K_2 q^3 + K_3 q^5 - \theta V = -N \ddot{x} + \frac{1}{2} \rho_a D_B L_B U^2 \sum_{i=1}^3 a_i \left(\frac{w_b + \psi(x)}{U} \right)^i, \quad (12)$$

$$\frac{1}{2} C_p V \dot{q} + \frac{V}{R} + \theta q = 0.$$

3. Simulations and analysis

In this part, the numerical simulation is carried out to investigate the influence of galloping on the response of bi-stable energy harvester under harmonic and random base excitations, respectively. **Table 1** summarizes the main model parameters used for simulations and experiments. The value of parameters can be obtained by measurement and calculation based on the geometric dimensions and properties of

materials.

Table 1 Physical and geometric properties of piezo-aeroelastic energy harvester

| Physic property and symbol | Value | Physic property and symbol | Value |
|--|-------------------------|---|--|
| Length of beam L | 0.15 m | Strain coefficient of piezoelectric layer e_{31} | -11.6 C.m ⁻² |
| Width of beam w_b | 0.015 m | Permittivity component of piezo-electric layer e_{33} | 3.18×10^{-8} nF.m ⁻¹ |
| Thickness of beam h_b | 4×10^{-4} m | Distance between magnets (a, d) | 0.022 m, 0.021 m |
| Young's modulus of Steel Y_b | 210 GPa | Volume of magnets $V_m(j=A, B, C)$ | 1.2×10^{-6} m ³ |
| Density of steel layer ρ_b | 7800 kg.m ⁻³ | Magnetization intensity $M_j(j=A, B, C)$ | 0.8×10^6 A m ⁻¹ |
| Length of piezoelectric layer L_p | 0.037 m | Diameter of bluff body D_B | 0.032 m |
| Thickness of piezoelectric layer h_p | 3×10^{-4} m | Length of bluff body L_B | 0.107 m |
| Width of piezoelectric layer w_p | 0.01 m | Mass of bluff body M_E | 0.004 kg |
| Density of piezoelectric layer ρ_p | 7700 kg.m ⁻³ | Mechanical damping ratio ξ | 0.005 |
| Young's modulus of Piezoelectric material C_{11}^E | 67 GPa | Aerodynamics coefficients (a_1, a_2, a_3) | 1.56, 0, -6.9 |

3.1 Harmonic excitations

First, the base excitation is assumed to be a harmonic one, i.e., $\ddot{x} = A_b \cos(2\pi ft)$, where A_b and f are the magnitude and frequency of excitation, respectively. As shown in **Figure 3**, the diagrams of bifurcation of frequency versus voltage are presented as the magnitude of base excitation is $A_b=0.25$ g. The black dot line in **Figure 3(a1-d1)** represents the diagram of bifurcation and the blue line represents the results of forward sweeping. The wind speeds are varied at $U=0$ m/s, $U=2$ m/s, $U=2.5$ m/s and $U=3.6$ m/s so as to characterize the effects of wind speed on the mechanical and electrical responses. Since no other electrical load is applied, the voltage of MFC is simulated in open-circuit conditions. **Figure 3(a3-d3)** shows the diagrams of spectral with color bars to emphasize the contribution of the frequency component.

For comparison, at first no wind is blowing, the structure is excited only by the base motion, the system oscillates around all equilibria and executes a large-amplitude periodic motion, until the excitation frequency reaches 11.4 Hz (**Figure 3(a1)**). Then, with the frequency increasing, the system returns to oscillate around one equilibrium. The spectrum from 5 Hz to 11.4 Hz indicates that there are the fundamental frequency and high order harmonic components (see **Figure 3(a3)**). For the wind speed of $U=2$

m/s, the system exhibits a broad bandwidth of 7.5 Hz (5 Hz~12.5 Hz), as shown in **Figure 3(b1-b3)**, and there appears a chaotic motion at $f=13$ Hz. Then, at $U=2.5$ m/s, as shown in **Figure 3(c1-c3)**, the range of frequency for chaos is extended to 18 Hz, so the voltage generated in this range is enhanced. When the wind speed increases to $U=3.6$ m/s, both the inter-well chaos response and intra-well response in the high-frequency range evolve into a quasi-periodic response, which can be verified from the diagram of bifurcation, as shown in **Figure 3(d1)**. Thus, it can be concluded that the introduction of wind and increase in wind speed are helpful for extending the bandwidth of inter-well oscillation.

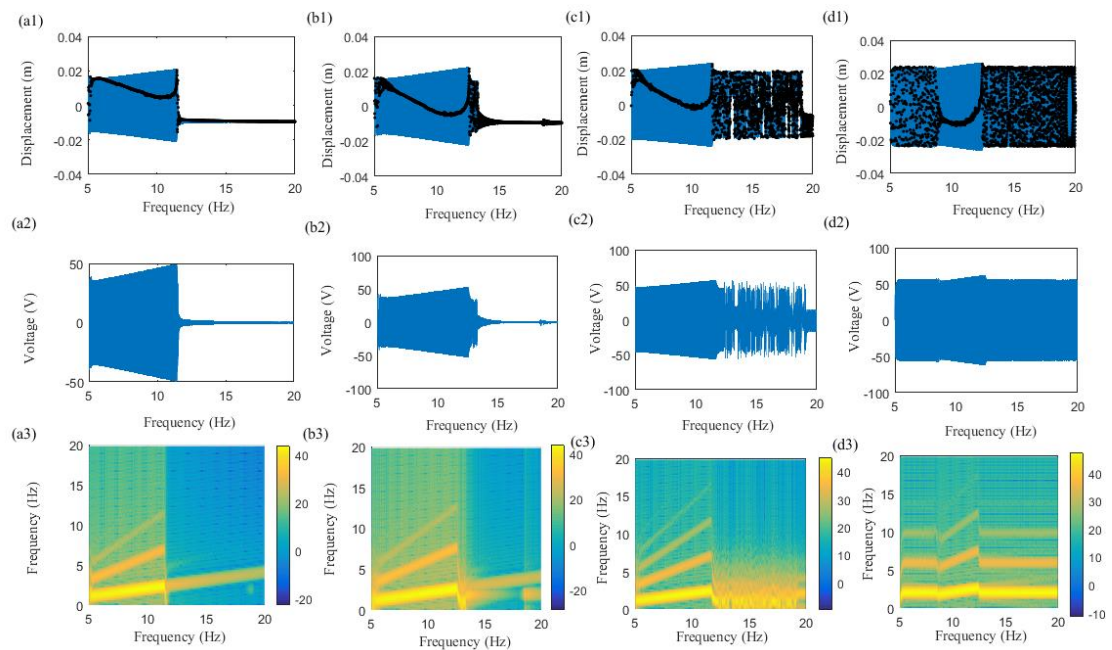


Figure 3. Simulated transient response under sweep excitation with a level of $A_b=0.25$ g. (a1-a3) $U=0$ m/s, (b1- b3) $U=2$ m/s, (c1-c3) $U=2.5$ m/s, (d1-d3) $U=3.6$ m/s.

In addition, **Figure 4** show the phase portraits with Poincaré sections for $U=0$ m/s, $U=2$ m/s, $U=2.5$ m/s and $U=3.6$ m/s at four excitation frequencies. The red points in these figures represent the Poincaré sections for determining the dynamical behaviors. In **Figure 4(a)**, when $f=8.5$ Hz, a periodic-1 inter-well motion circulating all stable equilibrium positions is demonstrated. Since the system's response will fall in a single potential well as the frequency exceeds 11.4 Hz, the responses at 13 Hz, 15 Hz and 18 Hz exhibit the intra-well periodic motions, as shown in **Figure 4(a1-a4)**. As the wind speed increases to 2 m/s, the system executes inter-well chaotic motions,

and it can be seen from **Figure 4(b)** that there is a strange attractor in the phase portraits, and some regular points appear in the Poincaré section. Then, as the frequency increase to 15 Hz, an intra-well period-5 response happens, as shown in **Figure 4(b3)**. Subsequently, the wind speed increases to $U=2.5$ m/s, the responses at 13 Hz, 15 Hz and 18 Hz all are the inter-well chaotic motions, as shown in **Figure 4(c)**. Then, when the wind speed increases to $U=3.6$ m/s, as shown in **Figure 4(d)**, the diagrams of Poincaré sections show a torus at 8.5 Hz, indicating the existence of a quasi-periodic motion. As the excited frequency increases to 13 Hz, the quasi-periodic responses evolve into a periodic response. When the excited frequency further increases and exceeds the jump-down frequency of 12.5 Hz, the response returns to the quasi-periodic motion at $f=15$ Hz and $f=18$ Hz, as shown in **Figure 4(d3, d4)**.

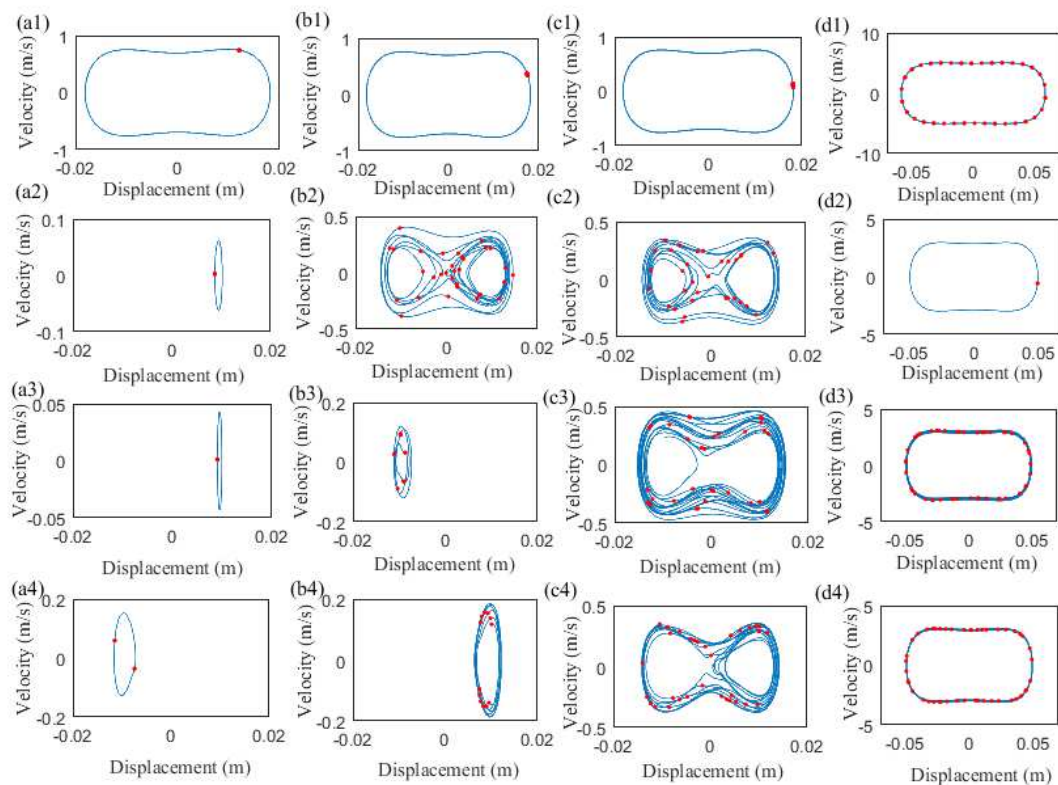


Figure 4. Phase portrait for setting the frequency of excitation as 8.5 Hz, 13 Hz, 15 Hz and 18 Hz, respectively. (a1-a4) $U=0$ m/s, (b1-b4) $U=2$ m/s, (c1-c4) $U=2.5$ m/s, (d1-d4) $U=3.6$ m/s.

The respective diagrams of simulated power spectral density are plotted in **Figure 5**. It should be noted that the PSDs' peaks at $U=3.6$ m/s are larger than that at

$U=0$ m/s in the entire frequency domain. If the system is only excited by the base excitation, as shown in **Figure 5(a, b, c)**, the vibration energy of periodic-1 response is concentrated to the integer multiple of the excitation frequency, while that of periodic-2 response is at one half of the integer multiple of excitation frequency, as **Figure 5(d)** shows. However, if a wind with the speed of $U=3.6$ m/s is introduced and combined with the base excitation, the response's PSD will own the extra frequency component induced by galloping. Especially, from the response shown in **Figure 5(a, c, d)**, it is clear that the effect of galloping could trigger the quasi-periodic motion and promote the efficiency of harvesting.

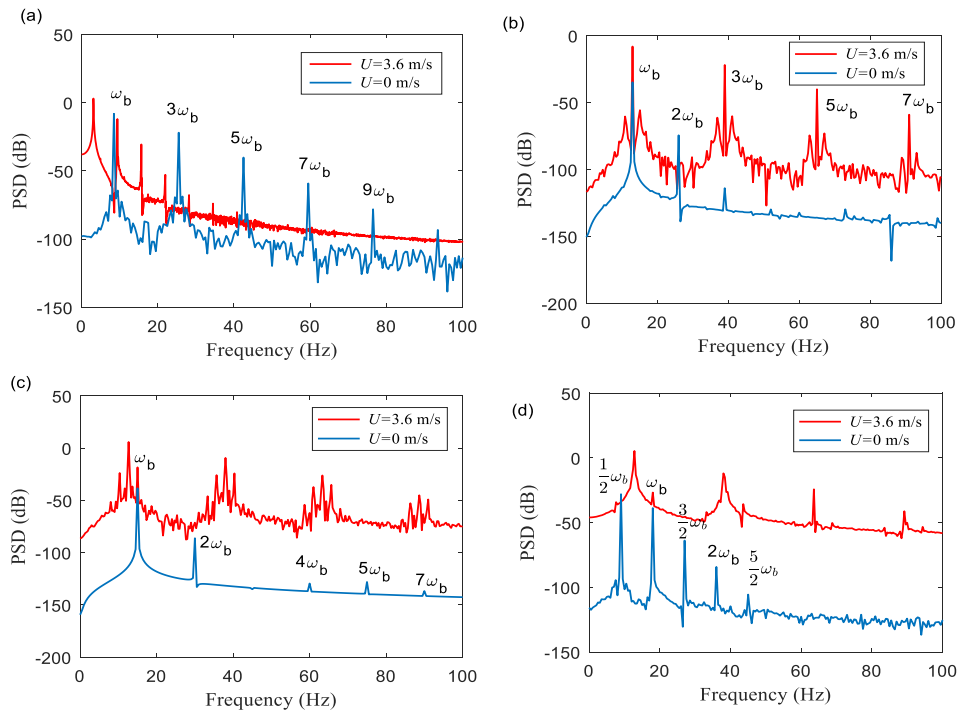


Figure 5. Power spectral density with the frequency of excitation for $A_b=0.25g$. (a) 8.5 Hz; (b) 13 Hz; (c) 15 Hz; (d) 18 Hz.

Next, three excitation levels, 0.25 g, 0.35 g and 0.45g are chosen so as to show the influence of base excitation level on the response. When the excitation acceleration is set to $A_b=0.25g$, as shown in **Figure 6(a1-a3)**, the forward frequency sweeping activates the periodic large-amplitude inter-well oscillations from the beginning of the frequency range, i.e., 5~12 Hz. As the frequency increases further, this large-amplitude oscillation gives way to the intra-well periodic oscillations. As **Figure**

6(b1-b3) shows, if the base acceleration increases to $A_b=0.35g$, the inter-well branch of oscillations exists over a wider range of frequencies, compared to that of $A_b=0.25g$. When the acceleration is further increased to $A_b=0.45g$, the input energy could lead the system to cross the potential barrier more easily. Thus, a more wider frequency range of inter-well motion, ranging from 5 Hz to 14 Hz, is formed, and more output is generated, as shown in **Figure 6(c1-c3)**.

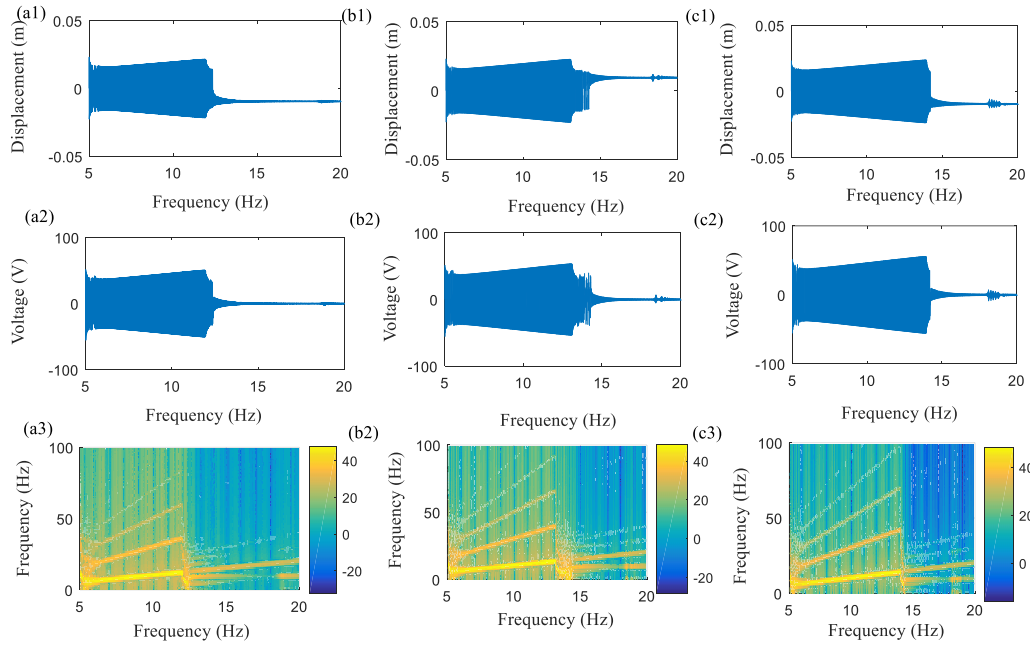


Figure 6. The effect of base excitation magnitude on the displacement and voltage. (a1-a3)

$A_b=0.25g$; (b1-b3) $A_b=0.35g$; (c1-c3) $A_b=0.45g$.

3.2 Random excitations

In fact, the ambient vibration always demonstrates non-stationary and broadband characteristics. Thus, to show its broadband characteristics more clearly, the proposed energy harvester is excited by random motions. A band-limited random excitation is obtained from a random test, as shown in **Figure 7**. The frequency of the random excitation is assumed to be uniformly distributed over a bandwidth of 5~50 Hz.

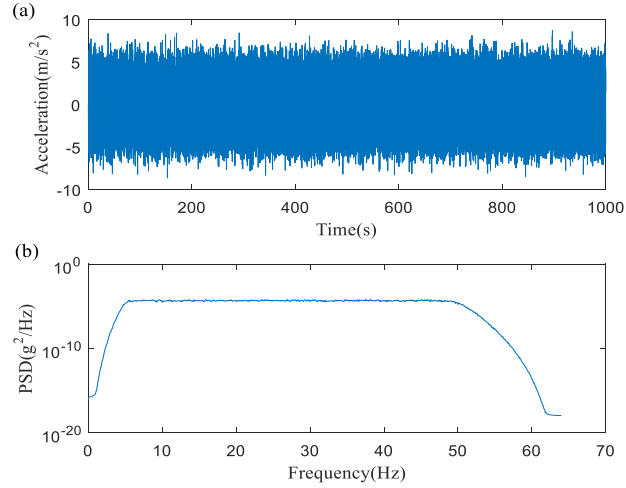


Figure 7. Band-limited random excitation. (a) Acceleration; (b) PSD of random excitation.

Figure 8(a) shows the diagrams of signal to noise ratio (R_{SNR} , it is denoted by $R_{\text{SNR}} = \sigma_q / D$ [8], where σ_q is the standard deviation of displacement, D is the power spectral density of random excitation.) and the RMS voltage. The bell shape curve of R_{SNR} implies the occurrence of stochastic coherence resonance, in which the system realizes a nearly regular jumping between the adjacent potential wells. To investigate the steady-state response, the system's simulated time is set to as long as 200 s. The peak or RMS value in random simulation is obtained by averaging over the time window with 20 full-time series. For $U=2$ m/s, the pronounced jump occurs at $D=0.5 \times 10^{-3}$ g²/Hz, while for $U=0$ m/s, it appears at $D=1.3 \times 10^{-3}$ g²/Hz. This indicates that the galloping contributes a lot and makes the system begin snap-through from a low-level random excitation. The nearly periodic jumping between the adjacent potential wells results in an instantaneous increase in output voltage. Thus, it can be concluded that the active galloping effect could help to increase the generated voltage, as shown in **Figure 8(b)**.

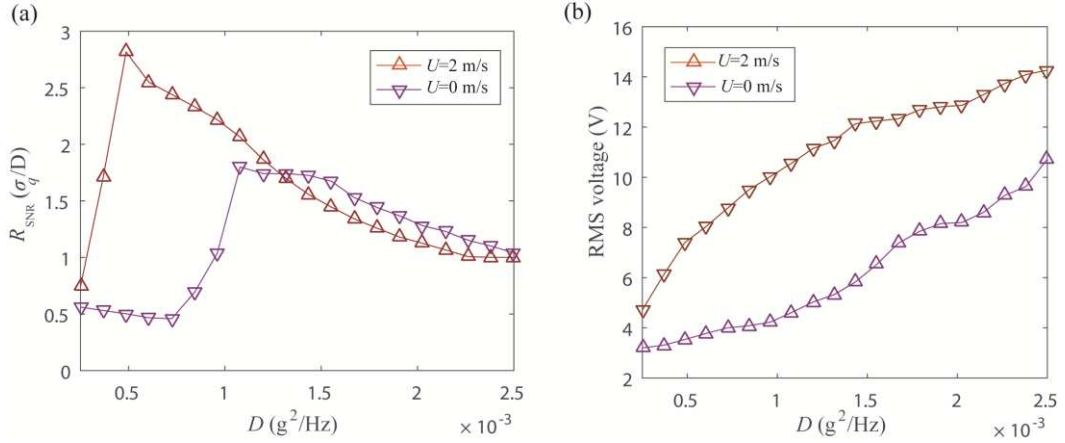


Figure 8. (a) R_{SNR} curve and (b) RMS voltage.

Figure 9(a1, b1, c1, d1) illustrates the time-domain response of the displacements and corresponding output voltages for $D=0.3 \times 10^{-3} g^2/Hz$. It can be seen that the jump between the adjacent potential wells does not occur for both $U=0$ m/s and $U=2$ m/s, and the response is restricted in a single potential well all the time. The RMS voltages for these two cases are 3.2 V and 4.8 V, respectively. Then, as D increases to $0.7 \times 10^{-3} g^2/Hz$, the jumping does not happen in the case without wind, i.e., $U=0$ m/s, and the output voltage is quite small. Then, if a galloping is introduced, e.g., $U=2$ m/s, the response demonstrates a jump between the adjacent potential wells and produces a large-amplitude displacement. Thus, a high output voltage is generated due to frequently jumping between the adjacent potential wells (see **Figure 9(c2, d2)**). The advantage of introducing galloping can be seen clearly from the comparison of RMS output voltages for the system for two cases of $U=0$ m/s and $U=2$ m/s, $V_{RMS}^{U=0} = 4.7$ V for the case without galloping and $V_{RMS}^{U=2} = 9.8$ V for the case with galloping, as shown in **Figure 9(b2, d2)**. Finally, as D increases to $1.7 \times 10^{-3} g^2/Hz$ and $2.5 \times 10^{-3} g^2/Hz$, a nearly regular jump between the adjacent potential wells, or coherence resonance, appears at both $U=0$ m/s and for $U=2$ m/s. But their amplitude is different. The galloping effect could lead the system to reach a frequently jumping between two potential wells (see **Figure 9(c3, d3, c4, d4)**), while for $U=0$ m/s the jumping seldom happens and the output voltage is relatively small (see **Figure 9(a3, b3, a4, b4)**). Therefore, compared to the system without galloping effect, a regular large-amplitude response is produced when it is subjected to the combined base excitation and galloping, and a denser high voltage is generated for the same level random excitation. It should be noted that the positive effects of galloping cannot be measured by peak-peak voltage if the random excitation level is large. Nevertheless,

the advantage of hybrid excitation can be characterized clearly from the RMS output voltages for the two situations, $V_{\text{RMS}}^{U=0} = 10.9 \text{ V}$ for the case without galloping and $V_{\text{RMS}}^{U=2} = 14.2 \text{ V}$ for the case with galloping effects, as shown in **Figure 9(b4, d4)**.

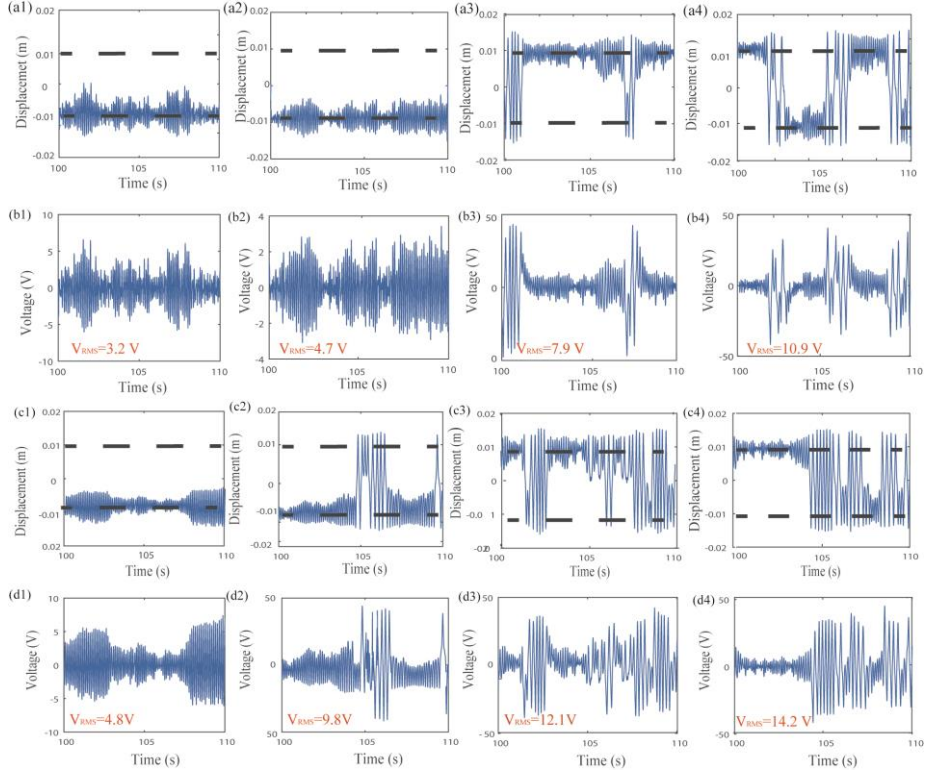


Figure 9. Simulated time histories of displacements and voltage. (a1, b1) $0.3 \times 10^{-3} \text{ g}^2/\text{Hz}$ for $U=0 \text{ m/s}$, (a2, b2) $0.9 \times 10^{-3} \text{ g}^2/\text{Hz}$ for $U=0 \text{ m/s}$, (a3, b3) $1.7 \times 10^{-3} \text{ g}^2/\text{Hz}$ for $U=0 \text{ m/s}$, (a4, b4) $2.5 \times 10^{-3} \text{ g}^2/\text{Hz}$ for $U=0 \text{ m/s}$. (c1, d1) $0.3 \times 10^{-3} \text{ g}^2/\text{Hz}$ for $U=2 \text{ m/s}$, (c2, d2) $0.9 \times 10^{-3} \text{ g}^2/\text{Hz}$ for $U=2 \text{ m/s}$, (c3, d3) $1.7 \times 10^{-3} \text{ g}^2/\text{Hz}$ for $U=2 \text{ m/s}$, (c4, d4) $2.5 \times 10^{-3} \text{ g}^2/\text{Hz}$ for $U=2 \text{ m/s}$.

4. Experimental findings

To verify the advantage of galloping predicted by the simulation, the validation experiment is conducted. The experimental setup is shown in **Figure 10**. In the experiment, the harvester consists of a steel cantilever beam, with a D-sectioned prism ($6 \text{ cm} \times 10 \text{ cm}$) attached to its free end. A NdFeB magnet was attached to the top of the beam and allowed to oscillate among two stationary NdFeB magnets mounted on the brackets. A piezoelectric Micro-fiber composite (MFC-M2807P2, Smart Material Corporation) was bonded to the beam. An electromagnetic shaker (LT-50, Econ Corp) was used to provide the base excitation and a wind tunnel was used to provide wind load. The wind speed was regulated by a frequency modulator and measured by an

anemometer (Bnetech, GM8903). An accelerometer (14100, Econ Corp) was used to measure the shaker's acceleration, and the signal was then fed back to the controller (VT-9008, Econ Corp) to control the vibration of shaker via a power amplifier. The dynamical response and output voltage signals was detected by the laser displacement sensor (OptoNCDT1620, Micro-Epsilon) and stored by the digital storage oscilloscope (MDO3024, Tektronix Company). The impedance of probe (Tektronix TPP0205) is about $10\text{ M}\Omega$ and thus the experiment is carried out in the open-circuit condition.

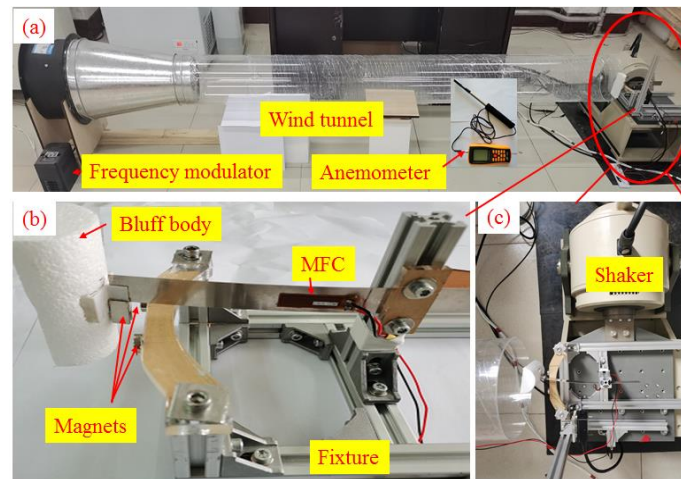


Figure 10. An overview of the experiment setup. (a) Wind tunnel and piezoelectric energy harvester fixed on the shaker; (b) Large version of piezoelectric energy harvester; (c) Overhead of piezoelectric energy harvester fixed on the shaker.

In the experiment, the base excitation was designed to sweep from 5 Hz to 25 Hz in both forward and backward directions. **Figure 11** shows the experimental transient responses under a sweeping base excitation of 0.25 g, while the wind speeds vary at $U=0\text{ m/s}$, $U=2\text{ m/s}$, $U=2.5\text{ m/s}$ and $U=3.6\text{ m/s}$, respectively. In **Figure 11**, the solid blue line represents the forward sweeping response, while the solid red line represents the backward one. The system responses at four wind speeds all exhibit the hysteretic frequency characteristic, due to which they bend toward the right. At $U=0\text{ m/s}$, i.e., there is no wind, as shown in **Figure 11(a1, b1)**, the forward sweeping frequency activates a large-amplitude oscillation over the range between 5 Hz and 10.4 Hz. Then, as the frequency increases, the high-energy solution will disappear and give way to the low-energy oscillation around the stable equilibrium. As for the backward

sweeping, the bandwidth for high-energy branch becomes narrower compared to the one of the forward sweeping, due to the hardening nonlinearity. Next, introducing the wind of $U=2$ m/s, the bandwidth of inter-well oscillation is extended to a wider range of frequency 6.4 Hz (from 5 Hz to 11.4 Hz), as shown in **Figure 11(a2, b2)**. Compared to the frequency response at $U=0$ m/s, the bandwidth of large-amplitude inter-well oscillation at $U=2$ m/s is extended by about 18.5%. Then, as the wind speed increases to $U=2.5$ m/s, the chaotic response appears and can keep over a wider range of frequency from 7.5 Hz to 18 Hz, and the system produces a large output voltage. Finally, as the wind speed reaches $U=3.6$ m/s, the bandwidth is extended to 12.5 Hz, and the intra-well oscillations in the high-frequency range are turned into the inter-well ones, thereby having a large amplitude. The forward sweeping experiment results are in good agreement with the simulations shown in **Figure 3**. Experimental results match well with the numerical results in jump down frequency and broadband inter-well band-width. The results demonstrate that as the wind speed increases, the area of less desirable small-amplitude intra-well branch will shrink, while that of the inter-well branch will extend. Therefore, it is experimentally validated that introducing galloping can extend the bandwidth of snap-through motion in the frequency domain such that it can harvest more energy for the wideband excitation.

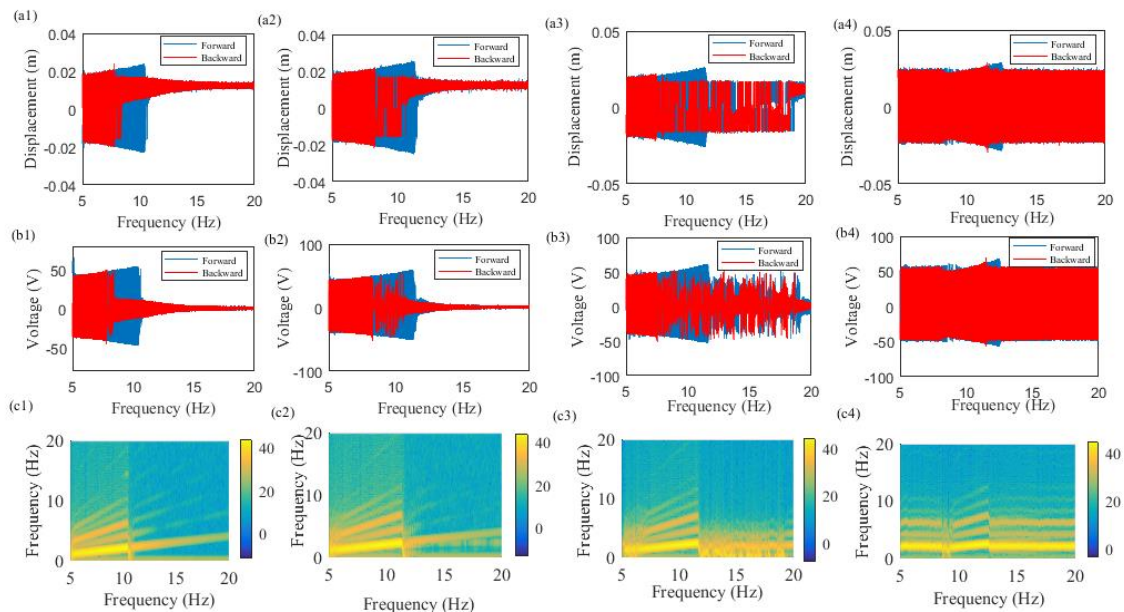


Figure 11. Experimental transient response under sweep excitation with a level of 0.25 g. (a1, b1) $U=0$ m/s, (a2, b2) $U=2$ m/s, (a3, b3) $U=2.5$ m/s, (a4, b4) $U=3.6$ m/s.

In the random validation experiments, a band-limited random excitation is set in the controller with a bandwidth of 5 Hz~50 Hz. Its intensity is varied from $0.3 \times 10^{-3} \text{ g}^2/\text{Hz}$ to $2.5 \times 10^{-3} \text{ g}^2/\text{Hz}$ sequentially. **Figure 12** compares the statistic characteristic of dynamics behaviors for $U=0 \text{ m/s}$ and $U=2 \text{ m/s}$, respectively. In **Figure 12(a)**, the curves of the standard deviation of displacement versus spectral density are plotted. It should be noted that the pronounced peaks imply the occurrence of a nearly regularly jumping between potential wells. The peak for the case with hybrid excitations ($U=2 \text{ m/s}$, $A_b = 0.25 \text{ g}$) appears at $D=0.5 \times 10^{-3} \text{ g}^2/\text{Hz}$, while that for the case with only base excitation ($U=0 \text{ m/s}$, $A_b = 0.25 \text{ g}$) appears at a much higher intensity of $D=1.1 \times 10^{-3} \text{ g}^2/\text{Hz}$.

Especially, the critical level obtained from the experiment is consistent with that from numerical simulation, as demonstrated in **Figure 8**. Both experimental and numerical results indicate that the introduction of wind can lead to the occurrence of coherence resonance at a lower random excitation level. Then, according to **Figure 12(b)**, compared to the output voltage at $U=0 \text{ m/s}$, i.e., the output voltage without galloping, it is evident that the bi-stable galloping energy harvester can generate more higher voltage at $U=2 \text{ m/s}$.

Figure 12(c, d) compares the time histories of the output voltage for $U=0 \text{ m/s}$ and $U=2 \text{ m/s}$, respectively. The experiment time in the random experiments is set to 200 s. When the excitation is fairly low, e.g., $D=0.3 \times 10^{-3} \text{ g}^2/\text{Hz}$, the peak-peak voltage is relatively low. The RMS voltage for the case without galloping is 3.1 V, while that for the case with galloping is 4.6 V. When the excitation increases to $D=0.9 \times 10^{-3} \text{ g}^2/\text{Hz}$, the voltage response at $U=2 \text{ m/s}$ realizes a sharp increase and the RMS voltage reaches 10 V, while the RMS voltage for the case without galloping is only about 5 V. As the excitation increases to the higher level, e.g., $D=1.7 \times 10^{-3} \text{ g}^2/\text{Hz}$ and $D=2.5 \times 10^{-3} \text{ g}^2/\text{Hz}$, a large-amplitude peak-peak voltage can be observed in both cases of $U=0 \text{ m/s}$ and $U=2 \text{ m/s}$. But at $U=2 \text{ m/s}$, the large peak-peak voltage appears more frequently. The simulated and measured RMS voltages at 12 excitation levels are listed in **Table 2**. The maximum error of RMS voltage is -13%, which is mainly caused by the random error in measurement. By summing the voltage under all excitation levels in **Table 2**, the total output voltage for all random excitation levels

can be obtained, which is increased by 53.4%.

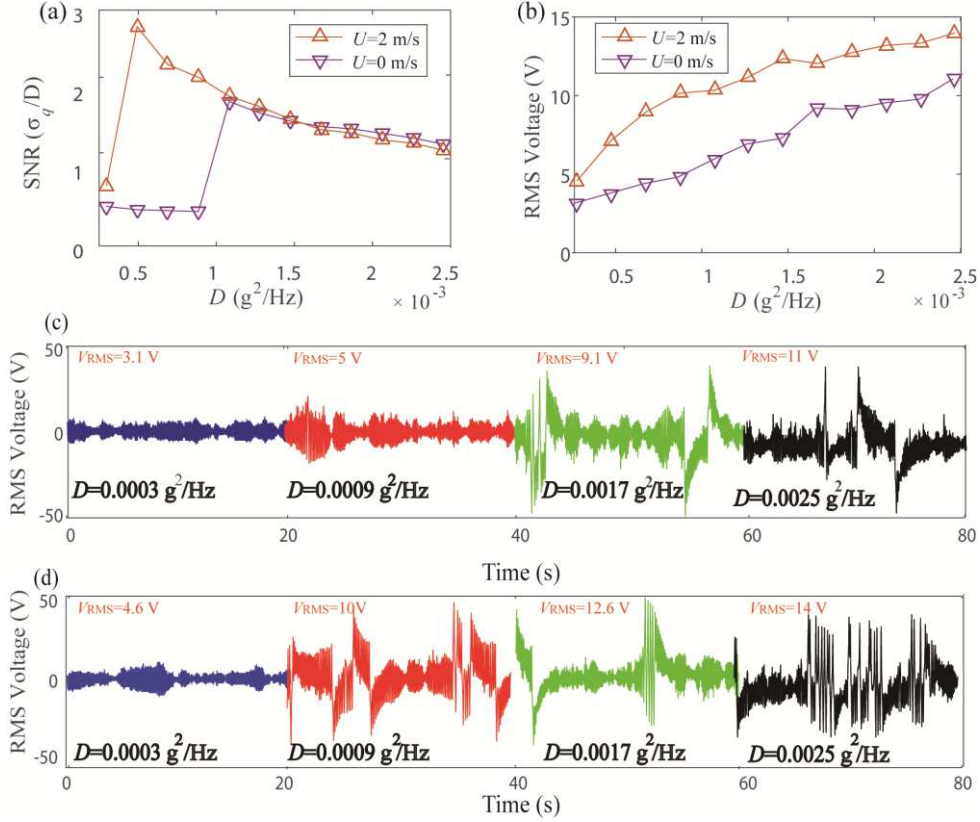


Figure 12. (a) Experimental standard deviation of dynamic displacement versus excitation intensity; (b) RMS voltage; (c, d) Experimental time-domain responses for $U=0$ and $U=2$ m/s, respectively.

Table 2. Comparison of simulated and measured RMS voltage under concurrent wind and random base excitation

| PSDs (g^2/Hz) | Simulated RMS voltage (V) | | Experimental RMS voltage (V) | | Error (%) | | PSDs (g^2/Hz) | Simulated RMS voltage (V) | | Experimental RMS voltage (V) | | Error (%) | |
|----------------------|------------------------------|-------|---------------------------------|-------|-----------|-------|----------------------|------------------------------|-------|---------------------------------|-------|-----------|-------|
| | $U=0$ | $U=2$ | $U=0$ | $U=2$ | $U=0$ | $U=2$ | | $U=0$ | $U=2$ | $U=0$ | $U=2$ | $U=0$ | $U=2$ |
| 0.0003 | 3.2 | 4.8 | 3.1 | 4.6 | +3% | +4% | 0.0015 | 6.8 | 12.1 | 7.3 | 12.3 | -7% | -1% |
| 0.0005 | 3.6 | 7.5 | 3.8 | 7.2 | -5% | +4% | 0.0017 | 7.9 | 12.1 | 9.1 | 12.6 | -13% | -4% |
| 0.0007 | 4 | 8.8 | 4.4 | 8.9 | -5% | -1% | 0.0019 | 8.2 | 12.5 | 9.2 | 12.7 | -12% | -2% |
| 0.0009 | 4.7 | 9.8 | 5 | 10 | -6% | +2% | 0.0021 | 12.9 | 13 | 9.5 | 13.2 | -3% | -2% |
| 0.0011 | 5.4 | 10.4 | 5.9 | 10.3 | -8% | +1% | 0.0023 | 9.3 | 13.5 | 9.8 | 13.4 | -5% | +1% |
| 0.0013 | 6 | 11.4 | 6.9 | 11.2 | -13% | +2% | 0.0025 | 10.9 | 14.2 | 11 | 14 | -1% | +1% |

The corresponding diagrams of power spectral density are plotted in **Figure 13**. As shown in **Figure 13(a)**, at $D=0.3 \times 10^{-3} g^2/Hz$, the PSDs for both the cases of $U=0$ m/s and $U=2$ m/s are relatively low. Then, in **Figure 13(b)**, the excitation increases to $D=0.9 \times 10^{-3} g^2/Hz$, since the response at $U=2$ m/s executes the snap-through motion, the PSD for $U=2$ m/s is obviously larger than the one for $U=0$ m/s in the

low-frequency range. Furthermore, as the excitation increases to $D=1.7 \times 10^{-3} \text{ g}^2/\text{Hz}$, the difference in PSDs for $U=0 \text{ m/s}$ and $U=2 \text{ m/s}$ becomes trivial, as shown in **Figure 13(c)**. Finally, as the excitation increases to $D=2.5 \times 10^{-3} \text{ g}^2/\text{Hz}$, the galloping effect becomes strong and could lead to the appearance of higher peaks in the low-frequency range, as shown in **Figure 13(d)**.

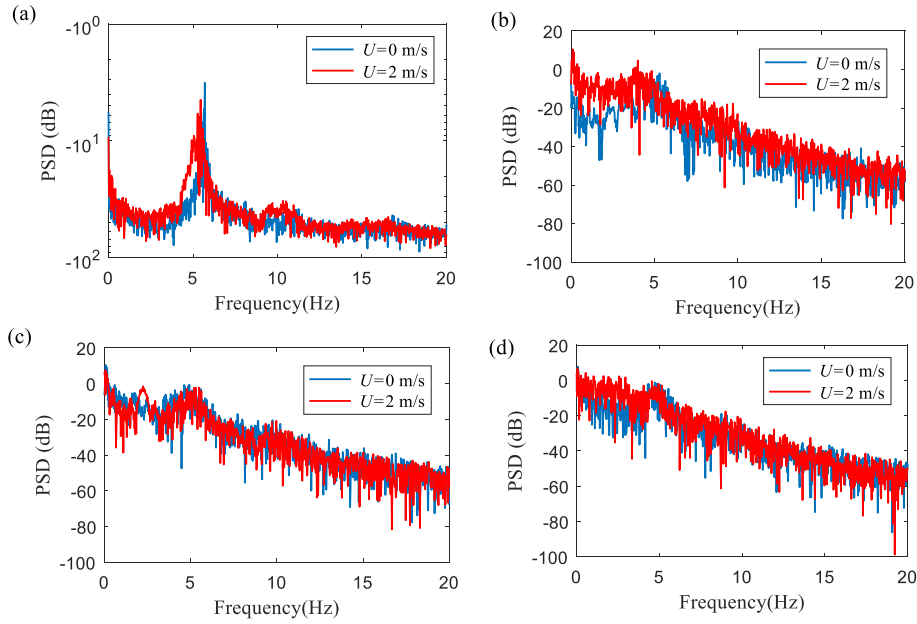


Figure 13. Frequency spectral density for random excitation levels. (a) $0.3 \times 10^{-3} \text{ g}^2/\text{Hz}$; (b) $0.9 \times 10^{-3} \text{ g}^2/\text{Hz}$; (c) $1.7 \times 10^{-3} \text{ g}^2/\text{Hz}$; (d) $2.5 \times 10^{-3} \text{ g}^2/\text{Hz}$.

5. Conclusions

In this paper, a bi-stable configuration is proposed to harvest both vibration energy and wind energy. From the simulation and experimental analyses, we can see that in this configuration the galloping and vibration effects could enhance each other and reach a high harvesting efficiency. From the analyses and experiments, following conclusions can be drawn.

(1) For the bi-stable energy harvester, if it is under the combined excitation of wind and harmonic vibration, the introduction of galloping could lead the large-amplitude inter-well motion more easily to be triggered in the high-frequency range. The bandwidth for the inter-well nonlinear dynamical behaviors, e.g., the

periodic, quasi-periodic or chaotic motion, will be extended with the increase of wind speed.

(2) Under the combined excitation of wind and random vibration, the introduction of galloping could decrease the critical excitation level for snap-through by 58%. Thus, the bi-stable energy harvester can execute snap-through from a low-level ambient excitation.

(3) The validation experiment results exhibit a good agreement with those predicted from theoretical analysis and simulations, confirming the advantage of the bi-stable energy harvester in harvesting wind and vibration energies. As a result, the total output voltage for all random excitation levels can increase by 53.4% averagely.

Acknowledgments

This work is financially supported by the National Natural Science Foundation of China (No.11902294).

Conflict of interest

The authors declare that they have no conflict of interest.

Data Availability Statements

The datasets generated during and/or analysed during the current study are available from the corresponding author on reasonable request.

Reference

- [1] Yang, Z., Zhou, S., Zu, J., Inman, D.: High-Performance Piezoelectric Energy Harvesters and Their Applications. *Joule*. **2** 642–697 (2018) <https://doi.org/10.1016/j.joule.2018.03.011>.

- [2] Daqaq, M.F., Masana, R., Erturk, A., Quinn, D.D.: On the role of nonlinearities in vibratory energy harvesting: a critical review and discussion. *Appl. Mech. Rev.* **66** 040801 (2014).
- [3] Wei, C., Jing, X.: A comprehensive review on vibration energy harvesting: Modelling and realization. *Renew. Sustain. Energy. Rev.* **74** 1-18 (2017). <https://doi.org/10.1016/j.rser.2017.01.073>.
- [4] Wang, L., Yuan, F.G.: Vibration energy harvesting by magnetostrictive material. *Smart. Mater. Struct.* **17** 1-18 (2008). <https://doi.org/10.1088/0964-1726/17/4/045009>.
- [5] Huynh, B.H., Tjahjowidodo, T., Zhong, Z.W., Wang, Y., Srikanth, N.: Design and experiment of controlled bistable vortex induced vibration energy harvesting systems operating in chaotic regions. *Mech. Syst. Signal. Process.* **98** 1097–1115 (2018) <https://doi.org/10.1016/j.ymsp.2017.06.002>.
- [6] Fu, Y., Ouyang, H., Benjamin, D.R.: Nonlinear structural dynamics of a new sliding-mode triboelectric energy harvester with multistability. *Nonlinear. Dyn.* **100** 1941–1962 (2020) <https://doi.org/10.1007/s11071-020-05645-z>.
- [7] Qian, F., Zhou, S., Zuo, L.: Approximate solutions and their stability of a broadband piezoelectric energy harvester with a tunable potential function. *Commun Nonlinear. Sci. Numer. Simul.* **80** 104984 (2020) <https://doi.org/10.1016/j.cnsns.2019.104984>.
- [8] Li, H.T., Qin, W.Y., Lan, C.B., Deng, W.Z., Zhou, Z.Y.: Dynamics and coherence resonance of tri-stable energy harvesting system. *Smart. Mater. Struct* **25** 015001 (2015) <https://doi.org/10.1088/0964-1726/25/1/015001>.
- [9] Lai, S.K., Wang, C., Zhang, L.H.: A nonlinear multi-stable piezomagnetoelastic harvester array for low-intensity, low-frequency, and broadband vibrations. *Mech. Syst. Signal. Process.* **122** 87–102 (2019) <https://doi.org/10.1016/j.ymsp.2018.12.020>.
- [10] Li, K., Yang, Z., Gu, Y., He, S., Zhou, S.: Nonlinear magnetic-coupled flutter-based aeroelastic energy harvester: Modeling, simulation and experimental

- verification. *Smart. Mater. Struct.* **28** 015020 (2019) <https://doi.org/10.1088/1361-665X/aaede3>.
- [11] Wang, G.X., Ding, H., Chen, L.Q.: Nonlinear normal modes and optimization of a square root nonlinear energy sink. *Nonlinear Dyn* **104** 1069–1096 (2021). <https://doi.org/10.1007/s11071-021-06334-1>
- [12] Chen, L.Q., Jiang, W.A.: Internal Resonance Energy Harvesting. *J. Appl. Mech. Trans. ASME* **82** 031004 (2015) <https://doi.org/10.1115/1.4029606>.
- [13] Yuan, T., Yang, J., Chen, L.Q.: Nonlinear characteristic of a circular composite plate energy harvester: experiments and simulations. *Nonlinear. Dyn.* **90** 2495–2506 (2017) <https://doi.org/10.1007/s11071-017-3815-4>.
- [14] Yuan, T., Yang, J., Chen, L.Q.: Nonlinear dynamics of a circular piezoelectric plate for vibratory energy harvesting. *Commun Nonlinear. Sci. Numer. Simul.* **59** 651–666 (2018) <https://doi.org/10.1016/j.cnsns.2017.12.010>.
- [15] Zhou, W., Wang, B., Lim, C.W., Yang, Z.: A distributed-parameter electromechanical coupling model for a segmented arc-shaped piezoelectric energy harvester, *Mech. Syst. Signal Process.* **146** 107005 (2020) <https://doi.org/10.1016/j.ymsp.2020.107005>.
- [16] Fan, K., Cai, M., Liu, H., Zhang, Y.: Capturing energy from ultra-low frequency vibrations and human motion through a monostable electromagnetic energy harvester. *Energy* **169** 356–368 (2019) <https://doi.org/10.1016/j.energy.2018.12.053>.
- [17] Wang, C., Zhang, Q., Wang, W.: Low-frequency wideband vibration energy harvesting by using frequency up-conversion and quin-stable nonlinearity. *J. Sound. Vib.* **399** 169–181 (2017) <https://doi.org/10.1016/j.jsv.2017.02.048>.
- [18] Vocca, H., Neri, I., Travasso, F., Gammaitoni, L.: Kinetic energy harvesting with bistable oscillators. *Appl. Energy.* **97** 771–776 (2012) <https://doi.org/10.1016/j.apenergy.2011.12.087>.
- [19] Li, H.T., Qin, W.Y., Zu, J., Yang, Z.: Modeling and experimental validation of a buckled compressive-mode piezoelectric energy harvester. *Nonlinear. Dyn.* **92** 1761–1780 (2018) <https://doi.org/10.1007/s11071-018-4160-y>.

- [20] Zhao, L.C., Zou, H.X., Yan, G., Zhang, W.M., Peng, Z.K., Meng, G.: Arbitrary-directional broadband vibration energy harvesting using magnetically coupled flexensional transducers. *Smart. Mater. Struct.* **27** 095010 (2018) <https://doi.org/10.1088/1361-665X/aad2c8>.
- [21] Yang, W., Towfighian., S.: A hybrid nonlinear vibration energy harvester. *Mech Syst Signal Process* **90** 317–33 (2017) <https://doi.org/10.1016/j.ymssp.2016.12.032>.
- [22] Lallart, M., Zhou, S., Yan, L., Yang, Z., Chen, Y.: Tailoring multistable vibrational energy harvesters for enhanced performance: theory and numerical investigation. *Nonlinear. Dyn.* **96** 1283–1301 (2019) <https://doi.org/10.1007/s11071-019-04853-6>.
- [23] Yang, T., Cao, Q., Li, Q., Qiu, H.: A multi-directional multi-stable device: modeling, experiment verification and applications, *Mech. Syst. Signal Process.* **146** 106986 (2020) <https://doi.org/10.1016/j.ymssp.2020.106986>.
- [24] Zhang, J., Yang, K., Li, R.: A bistable nonlinear electromagnetic actuator with elastic boundary for actuation performance improvement. *Nonlinear. Dyn.* **100** 3575–3596 (2020) <https://doi.org/10.1007/s11071-020-05748-7>.
- [25] Stanton, S.C., McGehee, C.C., Mann, B.P.: Nonlinear dynamics for broadband energy harvesting: Investigation of a bistable piezoelectric inertial generator. *Phys. D. Nonlinear. Phenom.* **239** 640-653 (2010) <https://doi.org/10.1016/j.physd.2010.01.019>.
- [26] Erturk, A., Hoffmann, J., Inman, D.J.: A piezomagnetoelastic structure for broadband vibration energy harvesting. *Appl. Phys. Lett.* **94** 254102 (2009) <https://doi.org/10.1063/1.3159815>.
- [27] Cao, J., Wang, W., Zhou, S., Inman, D.J., Lin, J.: Nonlinear time-varying potential bistable energy harvesting from human motion. *Appl. Phys. Lett.* **107** 143904 (2015) <https://doi.org/10.1063/1.4932947>.
- [28] Zhou, Z., Qin, W., Du, W., Zhu, P., Liu, Q.: Improving energy harvesting from random excitation by nonlinear flexible bi-stable energy harvester with a variable

- potential energy function, *Mech. Syst. Signal Process.* **115** 162-172 (2019) <https://doi.org/10.1016/j.ymsp.2018.06.003>.
- [29] Huang, D.M., Zhou, S.X., Yang, Z.C.: Resonance mechanism of nonlinear vibrational multistable energy harvesters under narrow-band stochastic parametric excitations. *Complexity*. 1050143 (2019)
- [30] Cottone, F., Gammaitoni, L., Vocca, H., Ferrari, M., Ferrari, V.: Piezoelectric buckled beams for random vibration energy harvesting. *Smart. Mater. Struct* **21** 035021 (2012) <https://doi.org/10.1088/0964-1726/21/3/035021>.
- [31] Zhao, S., Erturk, A.: Electroelastic modeling and experimental validations of piezoelectric energy harvesting from broadband random vibrations of cantilevered bimorphs. *Smart. Mater. Struct.* **2** 015002 (2013) <https://doi.org/10.1088/0964-1726/22/1/015002>.
- [32] Fang, S., Fu, X., Liao, W.H.: Asymmetric plucking bistable energy harvester: Modeling and experimental validation. *J. Sound. Vib.* **459** 114852 (2019) <https://doi.org/10.1016/j.jsv.2019.114852>.
- [33] Barrero-Gil, A., Alonso, G., Sanz-Andres, A.: Energy harvesting from transverse galloping. *J. Sound. Vib.* **329** 2873-2883 (2010) <https://doi.org/10.1016/j.jsv.2010.01.028>.
- [34] Abdelkefi, A., Yan, Z., Hajj, M.R.: Modeling and nonlinear analysis of piezoelectric energy harvesting from transverse galloping. *Smart. Mater. Struct.* **22** 025016 (2013) <https://doi.org/10.1088/0964-1726/22/2/025016>.
- [35] Li, H., Ding, H., Chen, L.: Chaos threshold of a multistable piezoelectric energy harvester subjected to wake-galloping. *Int. J. Bifurc. Chaos.* **29** 1950162 (2019) <https://doi.org/10.1142/S0218127419501621.3>
- [36] Tan, T., Hu, X., Yan, Z., Zhang, W.: Enhanced low-velocity wind energy harvesting from transverse galloping with super capacitor. *Energy* **187** 115915 (2019) <https://doi.org/10.1016/j.energy.2019.115915>.
- [37] Wang, J., Zhao, W., Su, Z., Zhang, G., Li, P., Yurchenko, D.: Enhancing vortex-induced vibrations of a cylinder with rod attachments for hydrokinetic

- power generation, *Mech. Syst. Signal Process.* **145** 106912 (2020) <https://doi.org/10.1016/j.ymssp.2020.106912>.
- [38] Tang, L., Zhao, L., Yang, Y., Lefeuvre, E.: Equivalent circuit representation and analysis of galloping-based wind energy harvesting. *IEEE/ASME Trans Mechatronics* **20** 834–844 (2015) <https://doi.org/10.1109/TMECH.2014.2308182>.
- [39] Javed, U., Abdelkefi, A.: Impacts of the aerodynamic force representation on the stability and performance of a galloping-based energy harvester. *J. Sound. Vib.* **400** 213–226 (2017) <https://doi.org/10.1016/j.jsv.2017.04.013>.
- [40] Dai, H.L., Abdelkefi, A., Javed, U., Wang, L.: Modeling and performance of electromagnetic energy harvesting from galloping oscillations. *Smart. Mater. Struct.* **24** 045012 (2015) <https://doi.org/10.1088/0964-1726/24/4/045012>.
- [41] Dai, H.L., Yang, Y.W., Abdelkefi, A., Wang, L.: Nonlinear analysis and characteristics of inductive galloping energy harvesters. *Commun. Nonlinear. Sci. Numer. Simul.* **59** 580–591 (2018) <https://doi.org/10.1016/j.cnsns.2017.12.009>.
- [42] Zhou, Z., Qin, W., Zhu, P., Shang, S.: Scavenging wind energy by a Y-shaped bi-stable energy harvester with curved wings. *Energy.* **153** 400–412 (2018) <https://doi.org/10.1016/j.energy.2018.04.035>.
- [43] Abdelmoula H., Abdelkefi A.: Investigations on the presence of electrical frequency on the characteristics of energy harvesters under base and galloping excitations. *Nonlinear. Dyn.* **89** 2461–2479 (2017) <https://doi.org/10.1007/s11071-017-3597-8>.
- [44] Bibo, A., Abdelkefi, A., Daqaq, M.F.: Modeling and characterization of a piezoelectric energy harvester under combined aerodynamic and base excitations. *J. Vib. Acoust Trans ASME* **137** 031017 (2015) <https://doi.org/10.1115/1.4029611>.
- [45] Bibo, A., Daqaq, M.F.: Energy harvesting under combined aerodynamic and base excitations. *J Sound Vib* **332** 5086–5102 (2013) <https://doi.org/10.1016/j.jsv.2013.04.009>.

- [46] Liu, H., Gao, X.: Vibration energy harvesting under concurrent base and flow excitations with internal resonance. *Nonlinear. Dyn.* **96** 1067–1081 (2019) <https://doi.org/10.1007/s11071-019-04839-4>.
- [47] Yan, Z., Abdelkefi, A.: Nonlinear characterization of concurrent energy harvesting from galloping and base excitations. *Nonlinear. Dyn.* **77** 1171–1189 (2014) <https://doi.org/10.1007/s11071-014-1369-2>.
- [48] Zhao, L., Yang, Y.: An impact-based broadband aeroelastic energy harvester for concurrent wind and base vibration energy harvesting. *Appl. Energy.* **212** 233–243 (2018) <https://doi.org/10.1016/j.apenergy.2017.12.042>.

Figures

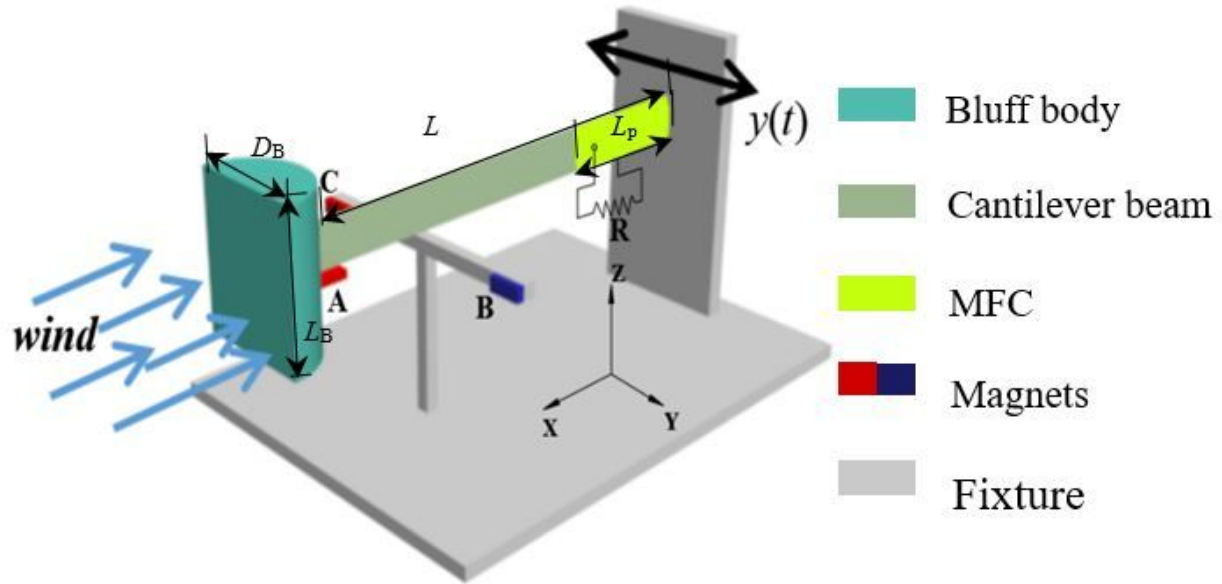


Figure 1

Configuration of proposed energy harvester subjected to concurrent wind and base excitation.

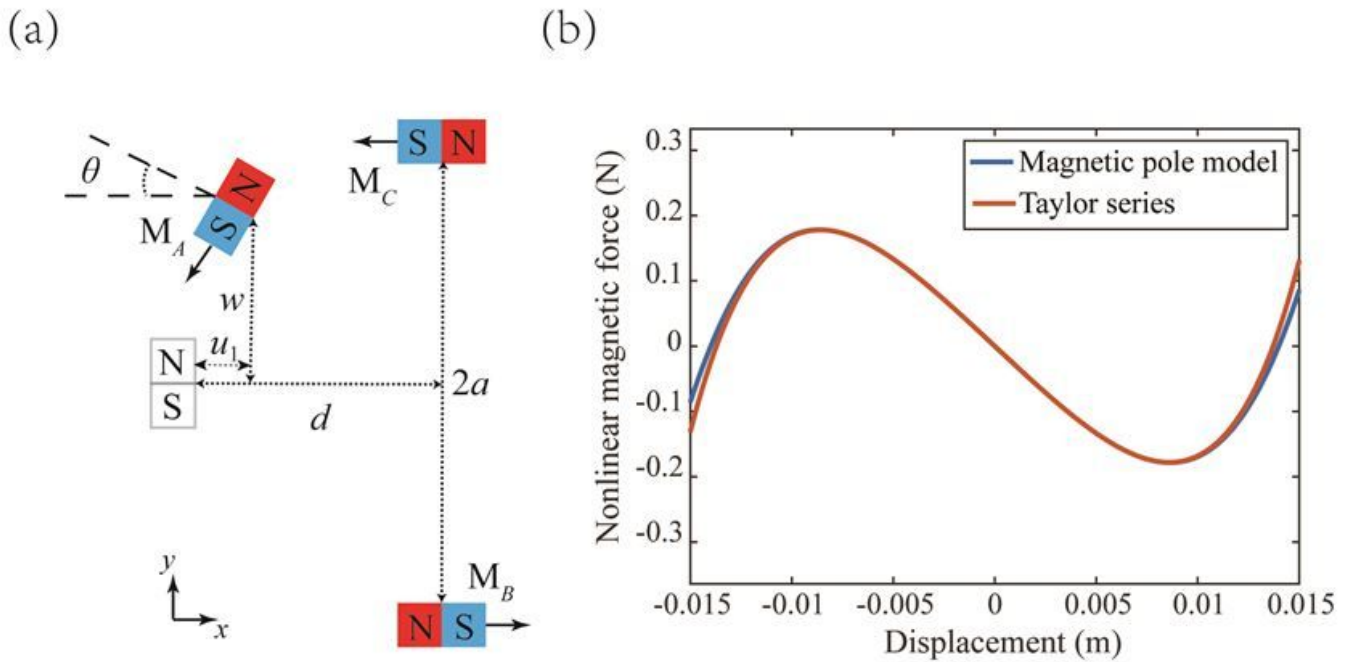


Figure 2

(a) Geometric diagram of magnetic dipoles; (b) Nonlinear magnetic force.

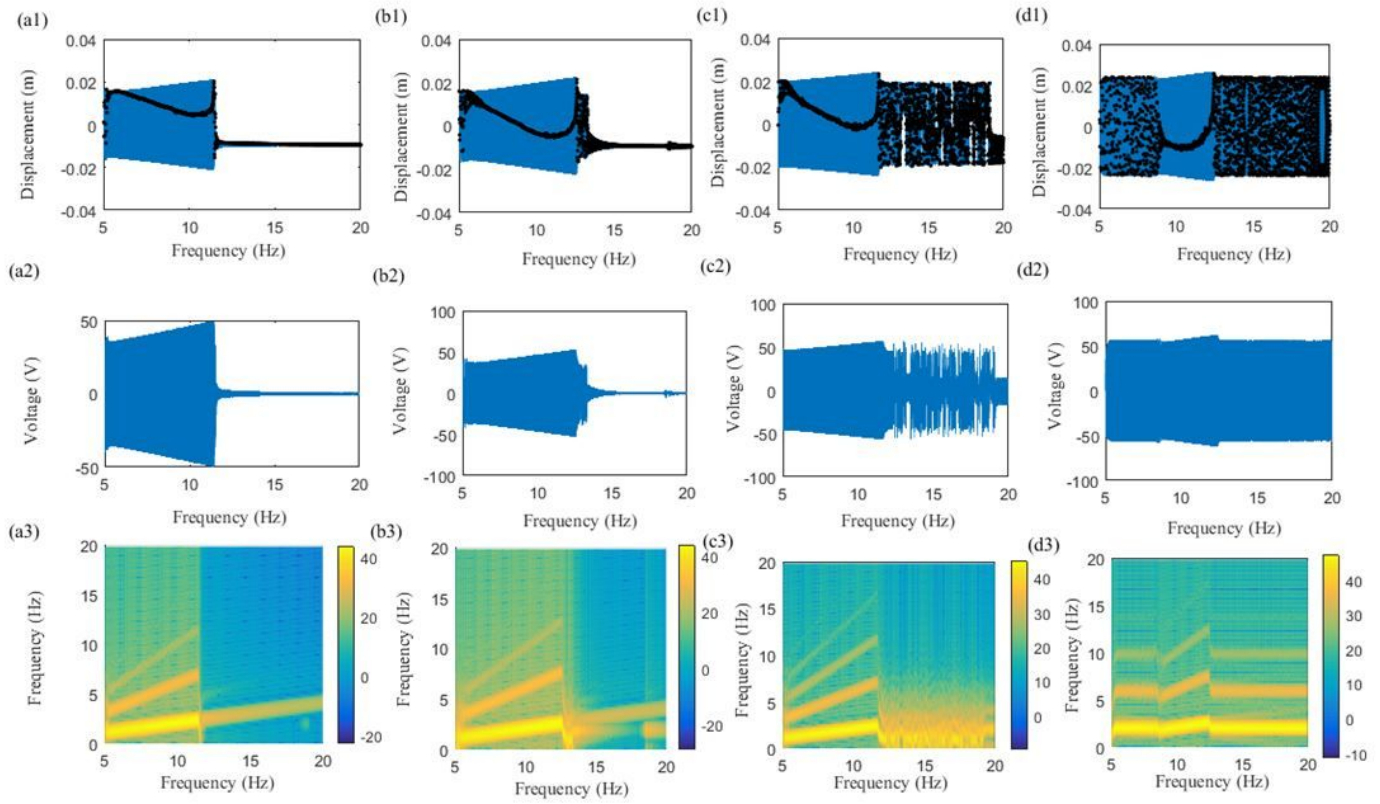


Figure 3

Simulated transient response under sweep excitation with a level of ≈ 0.25 g. (a1- a3) $U=0$ m/s, (b1- b3) $U=2$ m/s, (c1- c3) $U=2.5$ m/s, (d1- d3) $U=3.6$ m/s.

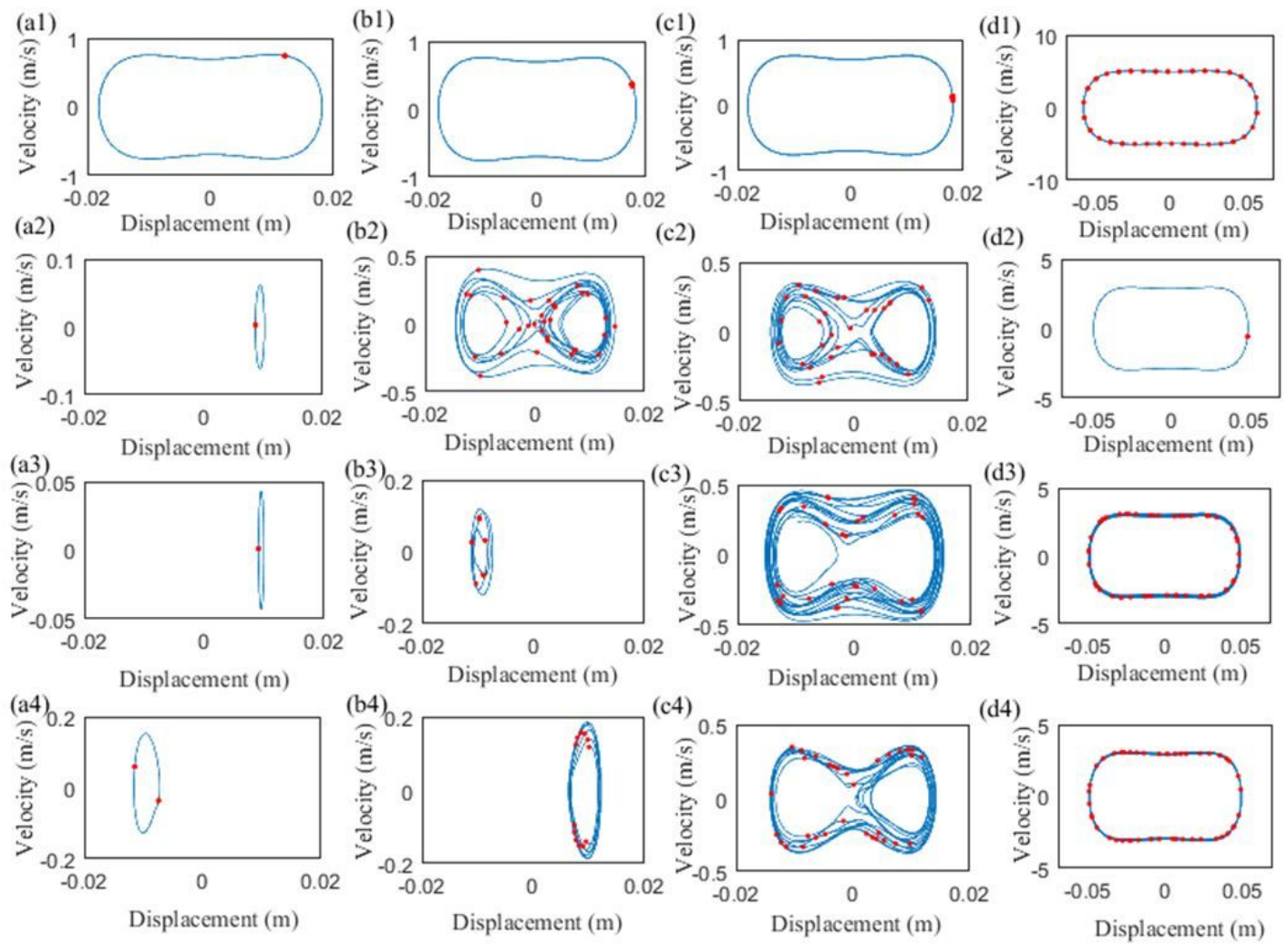


Figure 4

Phase portrait for setting the frequency of excitation as 8.5 Hz, 13 Hz, 15 Hz and 18 Hz, respectively. (a1-a4) $U=0$ m/s, (b1-b4) $U=2$ m/s, (c1-c4) $U=2.5$ m/s, (d1-d4) $U=3.6$ m/s.

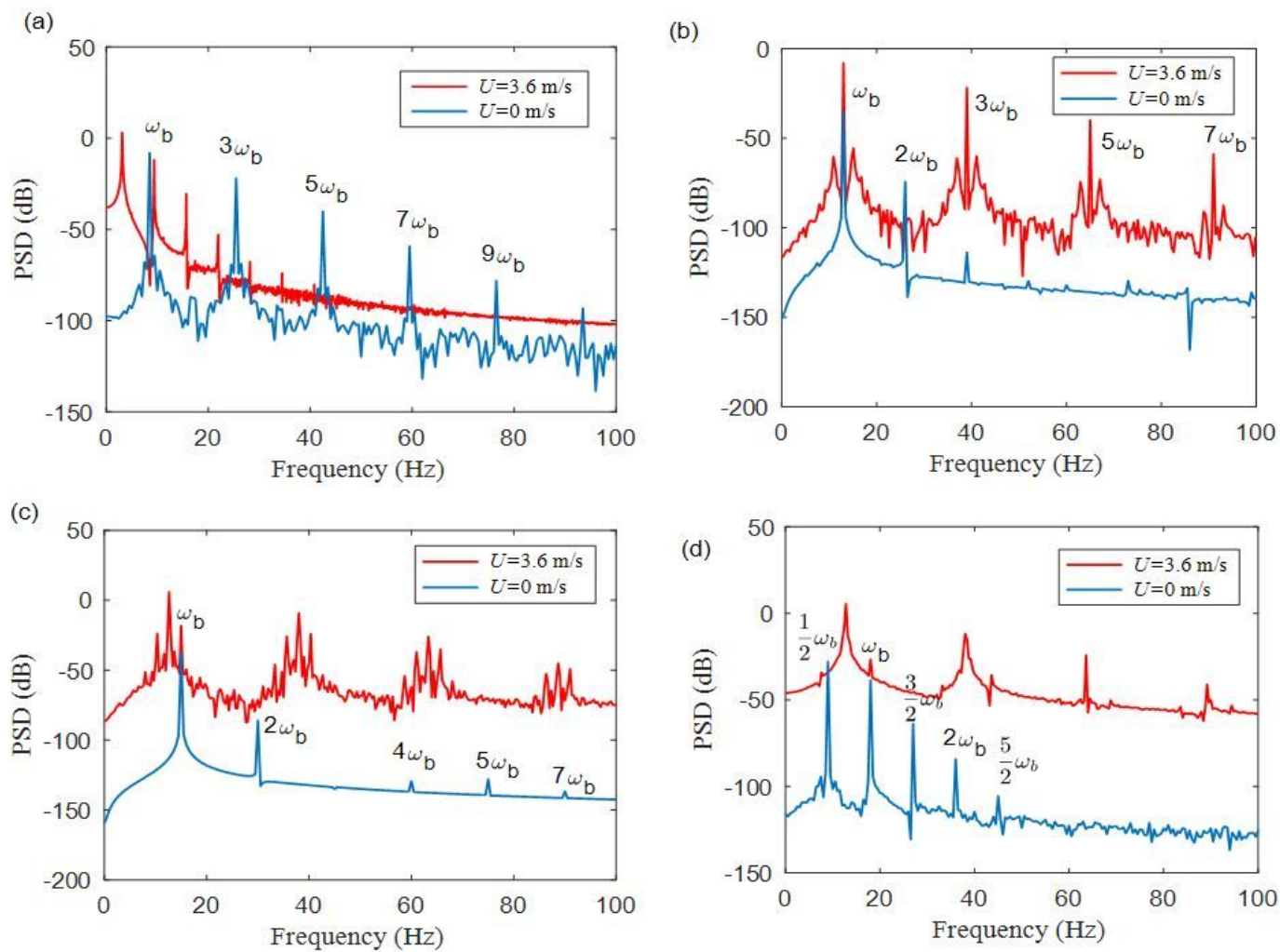


Figure 5

Power spectral density with the frequency of excitation for $A_b=0.25g$. (a) 8.5 Hz; (b) 13 Hz; (c) 15 Hz; (d) 18 Hz.

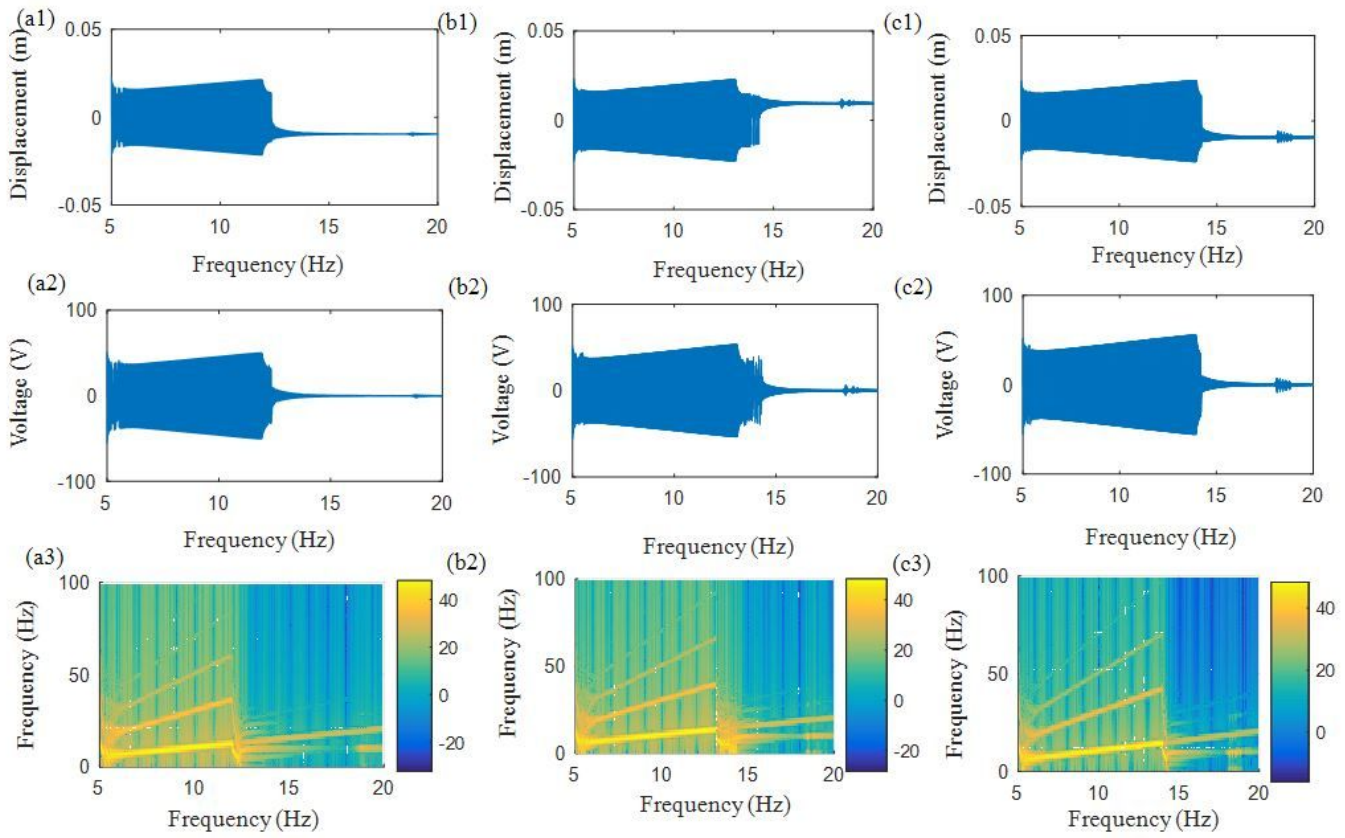


Figure 6

The effect of base excitation magnitude on the displacement and voltage. (a1-a3) $A_b=0.25g$; (b1-b3) $A_b=0.35g$; (c1-c3) $A_b=0.45g$.

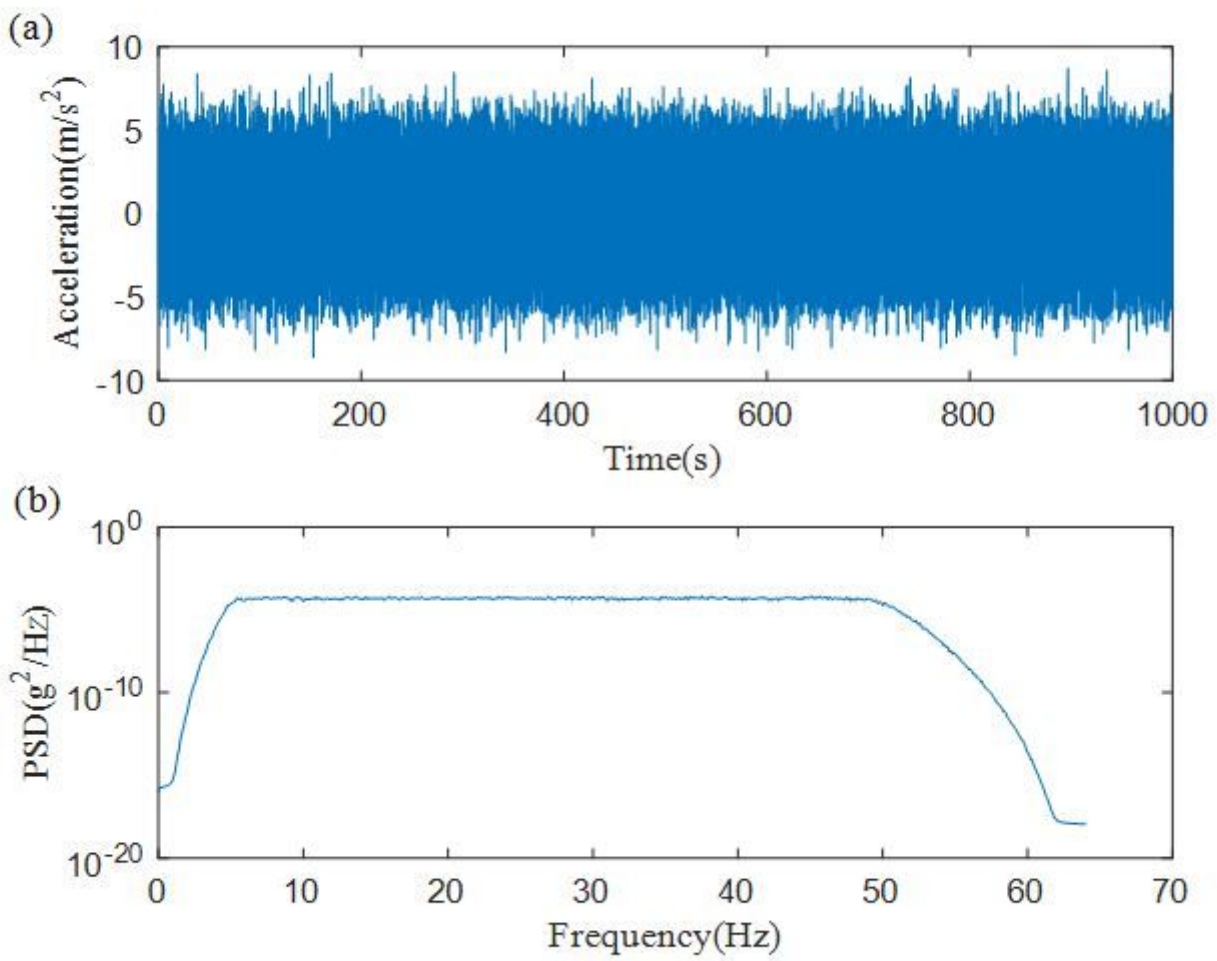


Figure 7

Band-limited random excitation. (a) Acceleration; (b) PSD of random excitation.

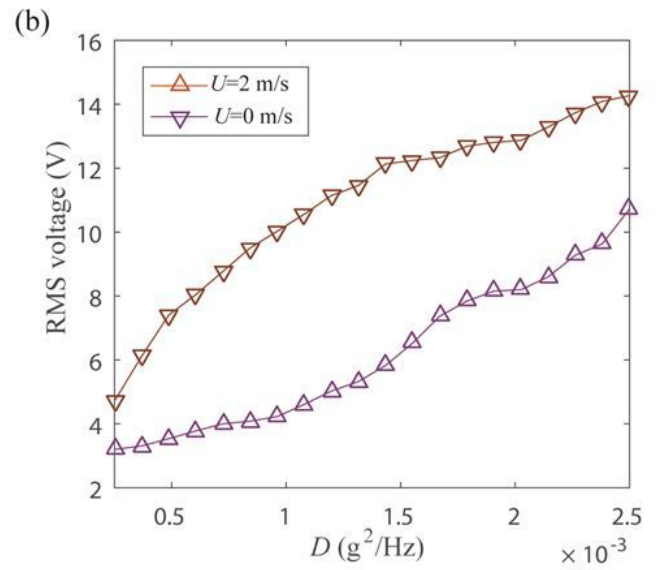
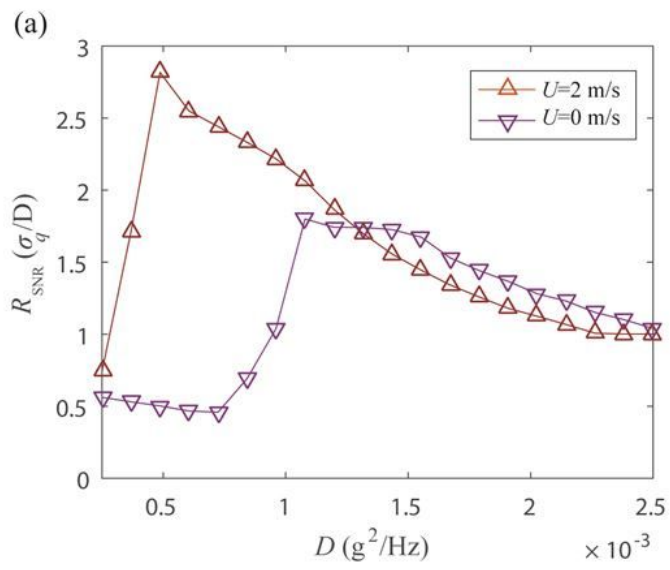


Figure 8

(a) RSNR curve and (b) RMS voltage.

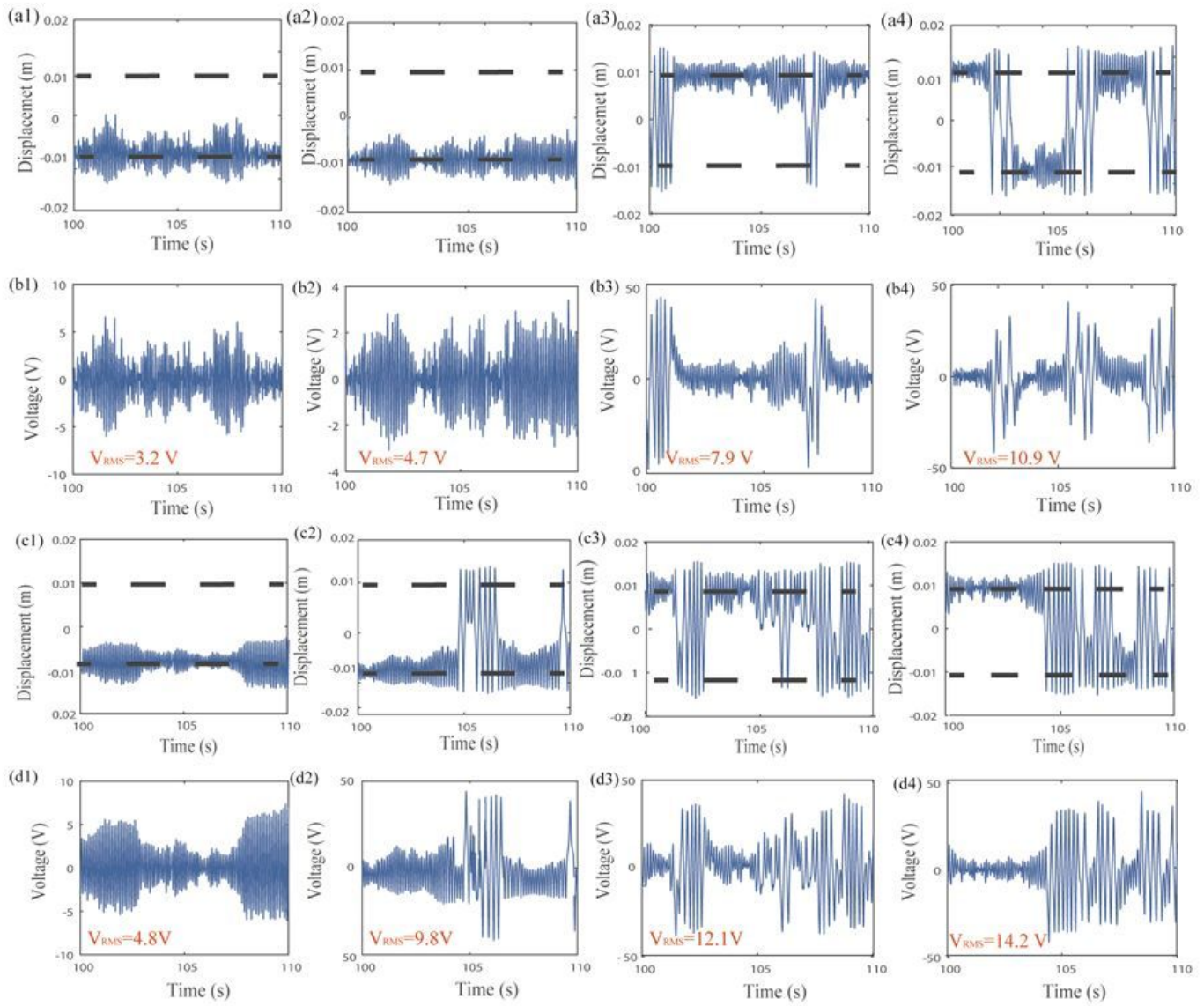


Figure 9

please see the manuscript file for the full caption

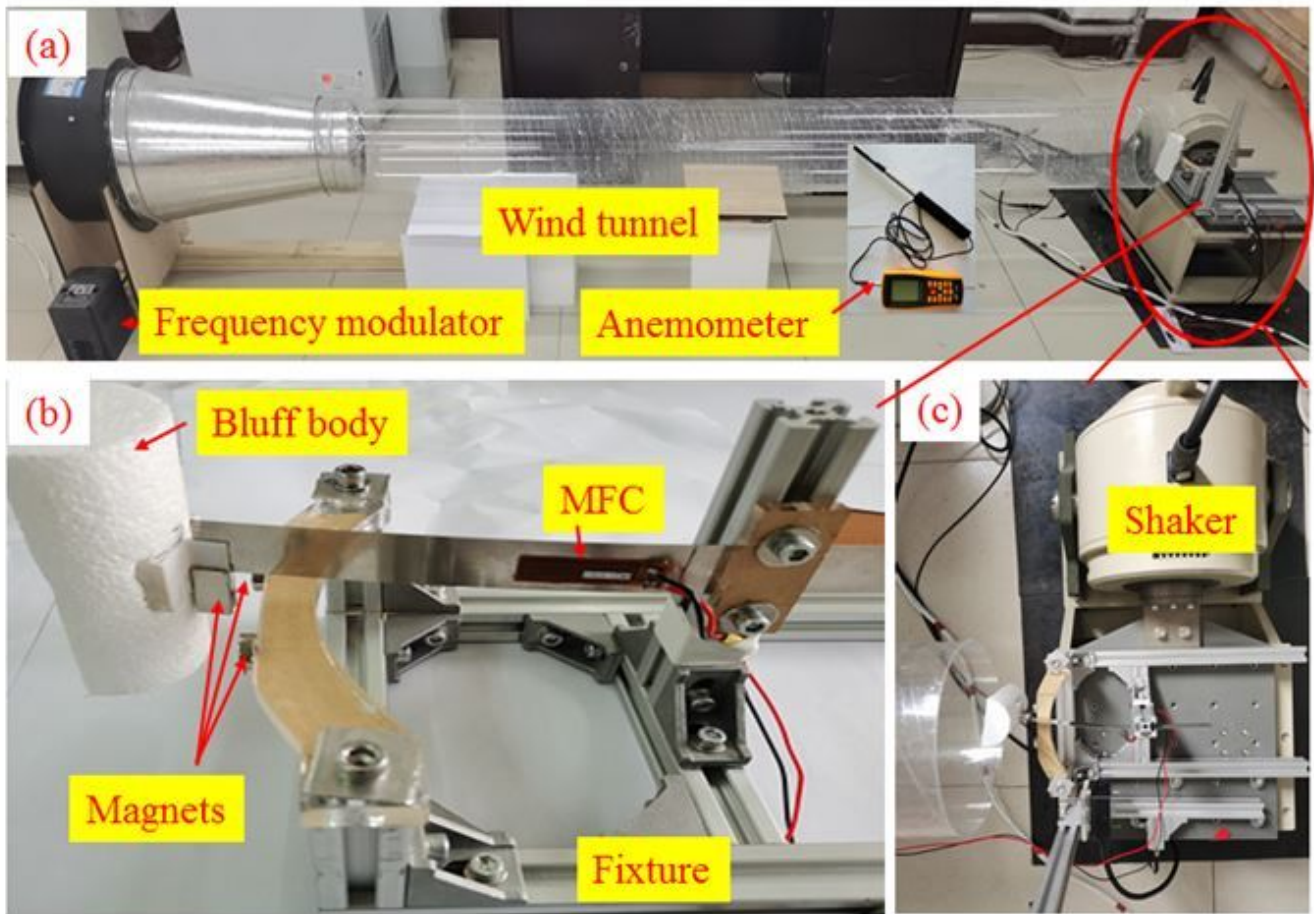


Figure 10

An overview of the experiment setup. (a) Wind tunnel and piezoelectric energy harvester fixed on the shaker; (b) Large version of piezoelectric energy harvester; (c) Overhead of piezoelectric energy harvester fixed on the shaker.

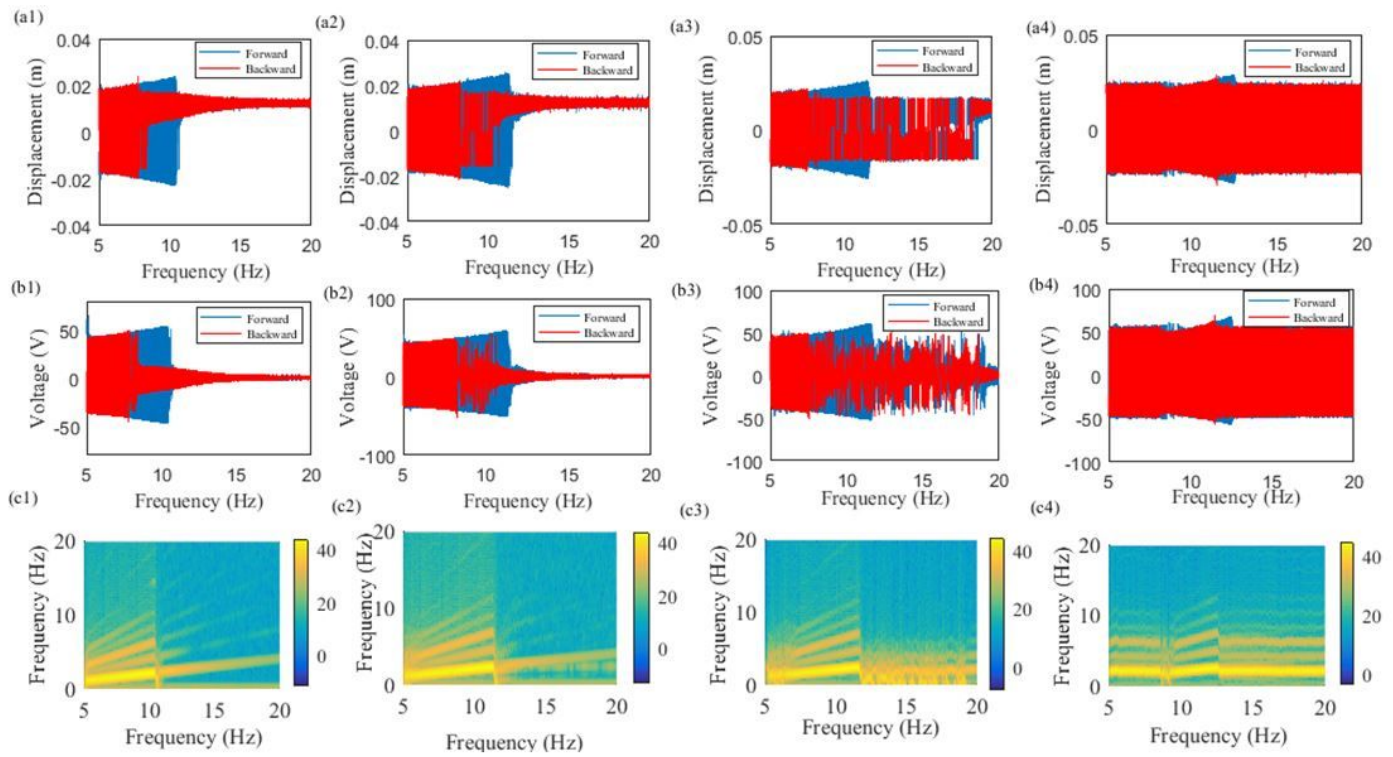


Figure 11

Experimental transient response under sweep excitation with a level of 0.25 g. (a1, b1) $U=0$ m/s, (a2, b2) $U=2$ m/s, (a3, b3) $U=2.5$ m/s, (a4, b4) $U=3.6$ m/s.

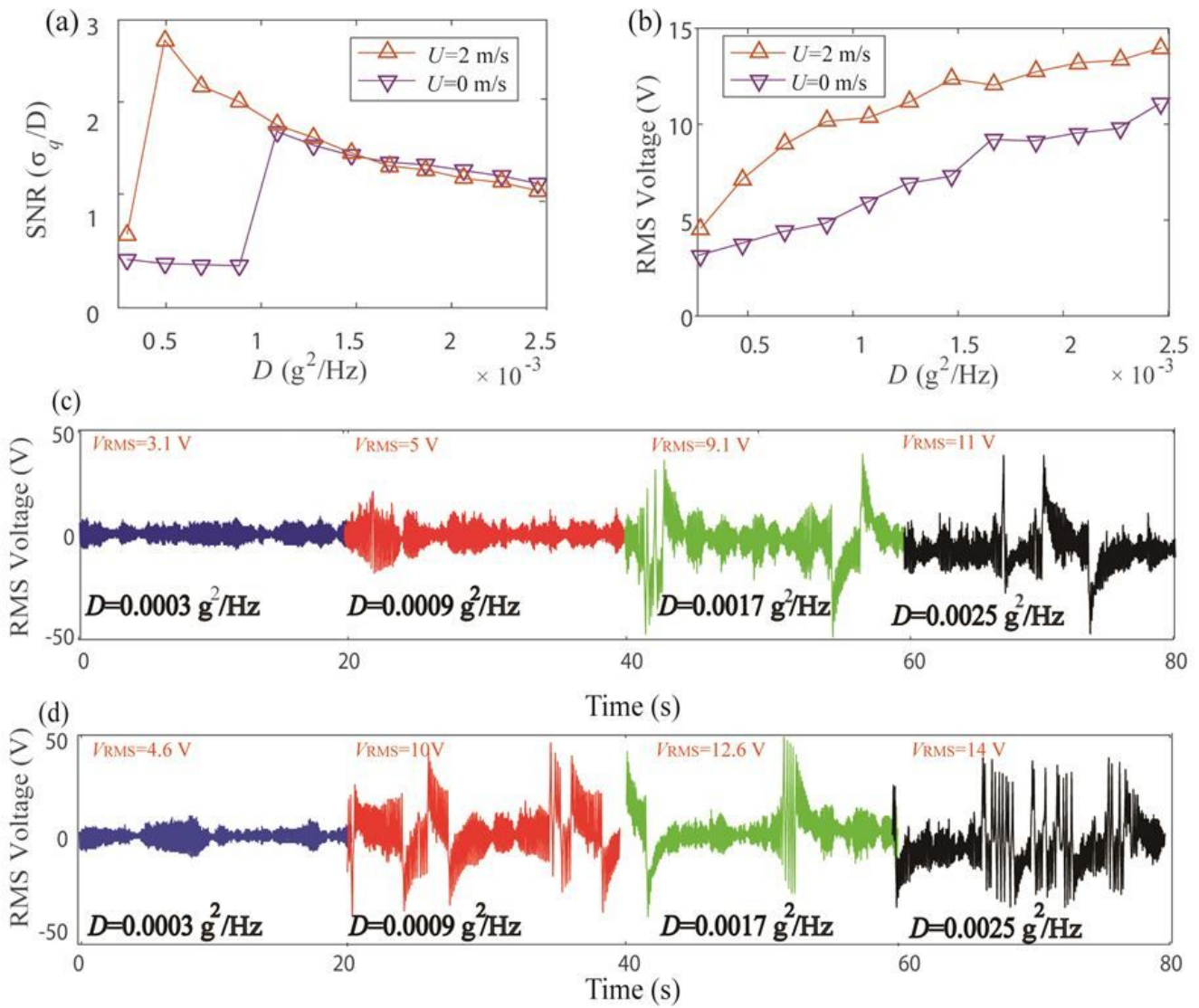


Figure 12

(a) Experimental standard deviation of dynamic displacement versus excitation intensity; (b) RMS voltage; (c, d) Experimental time-domain responses for $U=0$ and $U=2$ m/s, respectively.

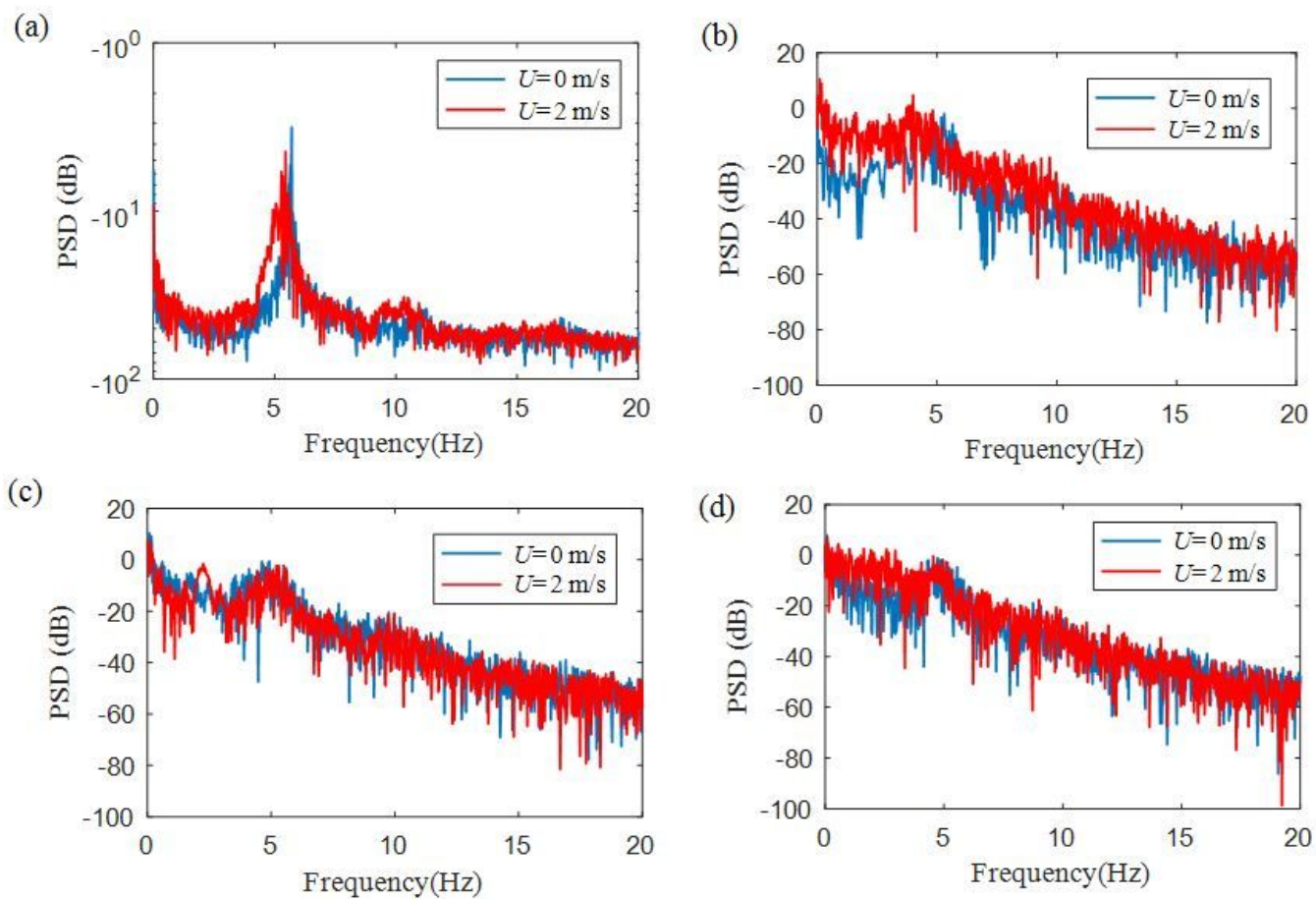


Figure 13

please see the manuscript file for the full caption